A Small-AC-Signal Injection Based Decentralized Secondary Voltage Control for Parallel Inverters With Accurate Reactive Power Sharing in Islanded Microgrids

Yidong Shi, *Student Member, IEEE*, Zeng Liu, *Senior Member, IEEE*, Jiazhi Wang, *Graduate Student Member, IEEE*, and Jinjun Liu, *Fellow, IEEE*

***Abstract*—To compensate for the voltage deviation at the point of common coupling (PCC) without communication links among distributed generations (DGs) in an islanded microgrid, proportional-integral regulator based secondary voltage control (PI-SVC) has been proposed in the literature. However, PI-SVC will degrade reactive power sharing performances, resulting from the activation time differences of secondary control. Moreover, PI-SVC may even cause reactive power divergence because of inaccurate estimated PCC voltages among DGs. To achieve precise PCC voltage restoration and maintain excellent reactive power sharing performance, this article proposes a small-ac-signal injection based secondary voltage control (SACS-SVC) in which an additional small-ac-signal (SACS) is injected into the output voltage of each DG. An additional positive droop relation is built between the injected SACS frequency and the voltage compensation value, which can be trimmed to be equal in each DG. As a result, PCC voltage deviations can be eliminated and reactive power sharing performances can be maintained. Meanwhile, the parameters of the proposed SACS-SVC are comprehensively designed through a small-signal differential mode model of the system. The effectiveness of the proposed method is demonstrated by the simulation and experimental results.**

***Index Terms*—Decentralized secondary control, microgrid, point of common coupling, signal injection.**

I. Introduction

With the expansion of renewable energy resources and increased environmental awareness, the use of microgrids is becoming a promising solution as a means of integrating different distributed generations (DGs) into power systems [1], which exhibits flexible controllability in both grid-connected and islanded modes. Parallel structured inverters are widely used in the hybrid photovoltaic microgrid [2], [3], [4] operating in islanded mode, as shown in Fig. 1, where the energy storage system consists of multiple inverters connected to a point of common coupling (PCC) through distribution cables and provide active and reactive power to the loads. Therefore, it is of vital importance to study the control methods of parallel inverters in the islanded microgrids.

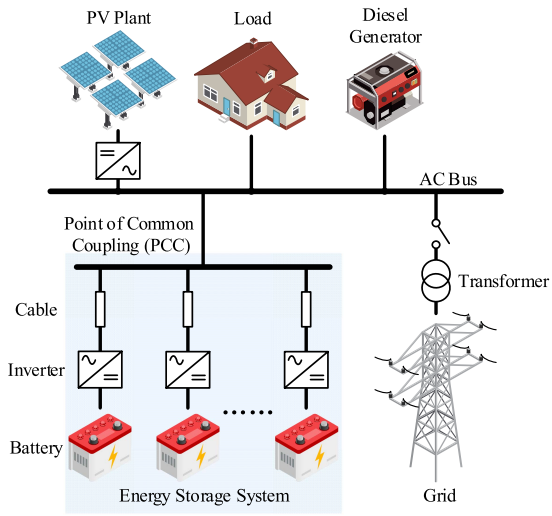

Fig. 1. Energy storage system with parallel inverters in a typical hybrid photovoltaic microgrid operating in islanded mode.

Droop control is widely applied to achieve equally active power sharing among DGs without communication links in the islanded microgrid. Although the mismatched feeder impedance will lead to poor reactive power sharing, it still can be improved by the virtual impedance [5], [6], [7]. However, the major drawback of droop control is the tradeoff between accurate power sharing and voltage regulation; i.e., the steeper the droop coefficient is set, the better the power sharing can be guaranteed, but it results in larger output voltage deviations in transients.

To eliminate frequency and amplitude deviations of voltage, extra control loops based on a hierarchical control architecture are integrated into the inverter [1], [8], [9], [10].

Manuscript received 29 August 2022; revised 16 December 2022, 5 March 2023, and 19 May 2023; accepted 1 July 2023. Date of publication 11 July 2023; date of current version 22 September 2023. This work was supported by the National Natural Science Foundation of China under Grant 51777160. Recommended for publication by Associate Editor L. Peng. *(Corresponding author: Zeng Liu.)*

The authors are with the State Key Laboratory of Electrical Insulation and Power Equipment, School of Electrical Engineering, Xi'an Jiaotong University, Xi'an 710049, China (e-mail: yidongshi@foxmail.com; zengliu@mail.xjtu.edu.cn; jiazhi_wang@outlook.com; jjliu@mail.xjtu.edu.cn).

Color versions of one or more figures in this article are available at https://doi.org/10.1109/TPEL.2023.3294228.

Digital Object Identifier 10.1109/TPEL.2023.3294228

In this architecture, droop control method is adopted in the primary control while the secondary control is responsible for the deviation compensation. In terms of secondary voltage control in microgrids, considerable research [11], [12], [13] has focused on DG's terminal voltage compensation, while other research aimed to compensate voltage at PCC. However, PCC voltage is usually the main concern because the loads are connected to the PCC. Therefore, maintaining the stability of PCC voltage would greatly enhance the power supply reliability of the islanded microgrids [14], [15].

Unlike voltage compensation at the DG terminal in which the local controller can directly measure the output voltage, the challenge confronting voltage compensation at the PCC is the difficulty for the local controller to measure PCC voltage because of the geographical distance between the DG terminal and the PCC in the microgrid. Existing secondary voltage control methods at the PCC can be further categorized into PCC voltage sampling-based and PCC voltage estimation-based methods according to the PCC voltage acquisition.

In the PCC voltage sampling-based methods, the PCC voltage is sampled and sent to each DG via communication links. In [16], [17], and [18], a central controller was deployed to measure the PCC voltage and generate the voltage compensation value by a proportional-integral (PI) regulator, which is then sent to the local controller via communication links. However, a single point of failure in the centralized schemes will decrease the reliability of the entire system. To reduce the dependency on the central controller, distributed methods only rely on communication among DGs. In [19], a consensus-based distributed cooperative control was proposed to achieve proportional power sharing, PCC voltage and frequency restoration via a communication network. A distributed optimal control was proposed in [20] to minimize the voltage deviations and achieve accurate power sharing, but massive computation was unavoidable. A proportional regulator based decentralized scheme proposed in [21] sampled the PCC voltage using the local controller. However, transmission delay was not considered and the voltage cannot be fully compensated. In summary, the PCC voltage sampling-based methods need communication links, resulting in high costs and low reliability.

In contrast, the PCC voltage estimation-based secondary voltage control method only requires the feeder impedance information to estimate the PCC voltage without communication links. A filtered tracking error-based decentralized method was proposed in [22] to regulate the PCC voltage and achieve proportional load power sharing. However, computation burden were heavy and unidirectional low-bandwidth communication links were still needed to update the parameters when the loads changed. To further simplify the secondary control algorithm and reduce the reliance on communication links, proportional-integral regulator based secondary voltage control (PI-SVC) with a decentralized scheme has been proposed in [23] and [24]. In this scheme, the estimated PCC voltage is used as the input of the PI regulator to generate the voltage compensation value. The PCC voltage can be precisely restored and the feeder impedance information is the only constant required.

However, PI-SVC has two limitations. On one hand, the different activation times of PI-SVC in each DG cause the integrators to generate different voltage compensation values. Because voltage compensation value can affect both voltage amplitude and output reactive power in droop control, different voltage compensation values can also lead to reactive power sharing deterioration. On the other hand, inaccurate feeder impedance information will lead to inaccurate estimated PCC voltage among DGs, which will cause stability issue during the voltage restoration process with PI-SVC. Specifically, the voltage compensation value of PI-SVC will continuously accumulate until the estimated PCC voltage equals to the nominal voltage because of the zero-steady-error feature of the PI regulator. However, because of the inaccurate feeder impedance, the estimated PCC voltage in each DG is different, so the integrator in PI-SVC of each DG will incessantly accumulate. Consequently, the voltage compensation values as well as the reactive power of DGs will diverge from each other, which causes system failure.

To tackle aforementioned limitations of PI-SVC, this article improved the PI-SVC into a small-ac-signal injection based secondary voltage control (SACS-SVC). The contributions of this article are summarized as follows.

1) The cause and effect of different activation times and inaccurate feeder impedance with PI-SVC are analyzed in detail and verified experimentally.
2) With a SACS voltage injected by each DG, the input of PI regulator for the secondary voltage control is synthesized by using the estimated PCC voltage and the SACS active power multiplied by a pair of weight coefficients. Moreover, an additional positive droop relation is built between the SACS frequency and the voltage compensation value, which can be trimmed to be equal in each DG to prevent reactive power from diverging and deteriorating.
3) A comprehensive parameter design for the proposed control scheme is presented based on a small-signal differential mode model of parallel DGs in an islanded microgrid.

The rest of this article is organized as follows. Section II reviews the basic operational principle of PI-SVC and its limitations. The proposed SACS-SVC is introduced in Section III. In Section IV, the modeling process and the parameter design methodology are presented. The simulation and experimental results based on the proposed SACS-SVC are presented to validate the theoretical analysis and the effectiveness of the proposed method in Section V. Finally, Section VI concludes this article.

II. System Architecture and Traditional PI-SVC

A simplified islanded microgrid with multiple DGs is shown in Fig. 2. Each DG consists of a dc-link, a three-phase inverter and an inductor–capacitor (*LC*) filter. The interfacing inverters and loads are connected to the PCC. R_i and L_i ($i = 1, 2, \ldots, n$) are the feeder resistance and inductance between the ith DG terminal bus and the PCC. The capacitor voltages u_{Cabc}, inductor currents i_{Labc}, and output currents i_{Oabc} are measured by the

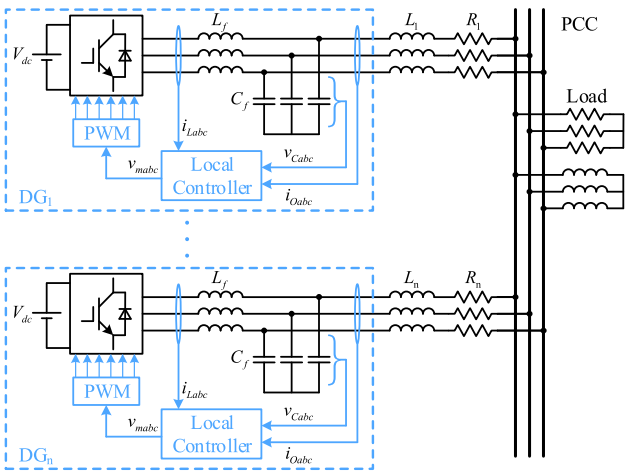

Fig. 2. Configuration of a simplified three-phase islanded microgrid system consisting of multiple DG units and a balanced load.

local controller to generate the pulsewidth modulation signal. The *LC* filter is used to suppress the switching harmonics of the output voltage.

The PI-SVC proposed in [23] and [24] is widely used, because it can compensate for the voltage deviations at the PCC without communication links. The PI-SVC can be expressed as follows:

$$E^* = E_0 - n(Q - Q_0) + \delta u \tag{1}$$

$$\delta u = \left(k_p + \frac{k_i}{s}\right)\left(U_{\mathrm{PCC0}} - \frac{\omega_{cv}}{s+\omega_{cv}} U_{\mathrm{PCC}Est}\right) \tag{2}$$

where E^* is the generated reference values of voltage amplitude, E_0 is the nominal voltage amplitude, Q is the output reactive power, Q_0 is the nominal reactive power, n is droop coefficient, δu is the voltage compensation value, k_p and k_i are the proportional and integral gains of the PI regulator, respectively, U_{PCC0} is the nominal PCC voltage, $U_{\mathrm{PCC}Est}$ is the estimated PCC voltage, and ω_{cv} is the cutoff angular frequency of the low-pass filter used in voltage estimation. Note that the feedback value of the PI regulator is the estimated PCC voltage rather than the real PCC voltage, which is calculated as

$$\begin{bmatrix} u_{\mathrm{PCC}Est\alpha} \\ u_{\mathrm{PCC}Est\beta} \end{bmatrix} = \begin{bmatrix} v_{C\alpha} \\ v_{C\beta} \end{bmatrix} - \begin{bmatrix} R_{mea} & -\omega_0 L_{mea} \\ \omega_0 L_{mea} & R_{mea} \end{bmatrix} \begin{bmatrix} i_{O\alpha} \\ i_{O\beta} \end{bmatrix} \tag{3}$$

$$U_{\mathrm{PCC}Est} = \sqrt{{u_{\mathrm{PCC}Est\alpha}}^2 + {u_{\mathrm{PCC}Est\beta}}^2} \tag{4}$$

where $U_{\mathrm{PCC}Est\alpha}$ and $U_{\mathrm{PCC}Est\beta}$ are the α-axis and β-axis components of the estimated PCC voltage, respectively, $v_{C\alpha}$ and $v_{C\beta}$ are the α-axis and β-axis components of the capacitor voltage, respectively, $i_{O\alpha}$ and $i_{O\beta}$ are the α-axis and β-axis components of the output current, respectively, and R_{mea} and L_{mea} are feeder impedances obtained by measurement [25], [26].

In addition, the virtual impedance is implemented to improve the reactive sharing performance based on the measured feeder impedance.

Sketched waveforms of the estimated PCC voltage, voltage compensation value, and reactive power of two DGs during the voltage restoration process with PI-SVC are shown in Fig. 3(a). PI-SVC of two DGs was implemented at $t = t_1$, then voltage compensation values were generated and the PCC voltage increased until it was fully restored at $t = t_2$. Specifically, the difference between the estimated PCC voltage and the PCC nominal voltage was sent to the PI regulator to generate the voltage compensation value, which was added to the *Q–E* droop control to tune the output voltage of the DG until the difference equaled to zero. The detailed operation principle of PI-SVC has been clearly discussed in [27].

A. Effect of Activation Time Difference on PI-SVC

Although PI-SVC can fully restore the PCC voltage, the reactive power sharing performance will be deteriorated during the voltage restoration process. To guarantee accurate reactive power sharing, the voltage compensation value δu must be the same for all the DGs. However, the δu, which is the output of the PI regulator, will differ from each other because of the different activation times of secondary control. The aforementioned limitation is demonstrated by implementing PI-SVC at different times for each DG, as shown in Fig. 3(b). At first, the estimated PCC voltage is lower than its nominal value and only DG_1 implements PI-SVC at $t = t_1$. The input of the PI regulator is positive, so δu value of DG_1 increases, causing the estimated PCC voltage and reactive power of DG_1 to increase, while the reactive power of DG_2 decreases because the total reactive power is unchanged. However, the secondary control of DG_2 shows a delay and is enabled at $t = t_2$. Then, the δu and reactive power of DG_2 start to increase until the PCC voltage is full restored at $t = t_3$. The different activation times of PI-SVC lead to the differences in δu values, which further deteriorates reactive power sharing performances.

B. Effect of Inaccurate Feeder Impedance on PI-SVC

In Fig. 3(a), the feeder impedance is accurate, thus the estimated PCC voltage ($U_{\mathrm{PCC}Est}$) is the same for both DGs and equals to the real PCC voltage. However, inevitable errors exist in the feeder impedance information due to measurement error in practical applications, leading to inaccurate estimated PCC voltages among DGs [28], [29]. If we consider the feeder impedance to be inaccurate, another problem arises: In this situation, the estimations of the unique PCC voltage of each DG will be different, which means that $U_{\mathrm{PCC}Est}$ values are no longer the same for parallel DGs.

Assume the $U_{\mathrm{PCC}Est}$ of DG_2 is greater than that of DG_1 and the activation time is the same for two DGs, the sketched waveforms are shown in Fig. 3(c). At first, PI-SVC was implemented at $t = t_1$, and the $U_{\mathrm{PCC}Est}$ values for both DGs are smaller than the nominal value. The inputs of both PI regulators are positive so that δu increases. The only difference is that the input of DG_1 is greater than that of DG_2 because the $U_{\mathrm{PCC}Est}$ value of DG_1 is smaller than that of DG_2, so δu of DG_1 will be slightly higher than that of DG_2. Then, as the PCC voltage increases, $U_{\mathrm{PCC}Est}$ of DG_2 reaches its nominal value at $t = t_2$, so the integrator of DG_2 stops. However, $U_{\mathrm{PCC}Est}$ of DG_1 is still less than the nominal value, hence, the integrator continues to accumulate, resulting in increases in the PCC voltage as well

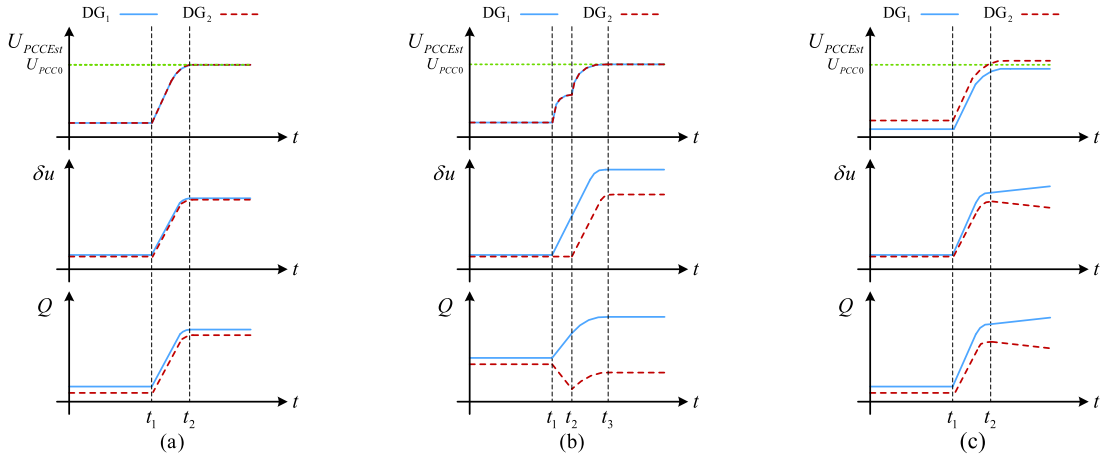

Fig. 3. Sketched waveforms of the estimated PCC voltage, voltage compensation value, and reactive power of two DGs. (a) PI-SVC with accurate feeder impedance. (b) PI-SVC with different activation times. (c) PI-SVC with inaccurate feeder impedance.

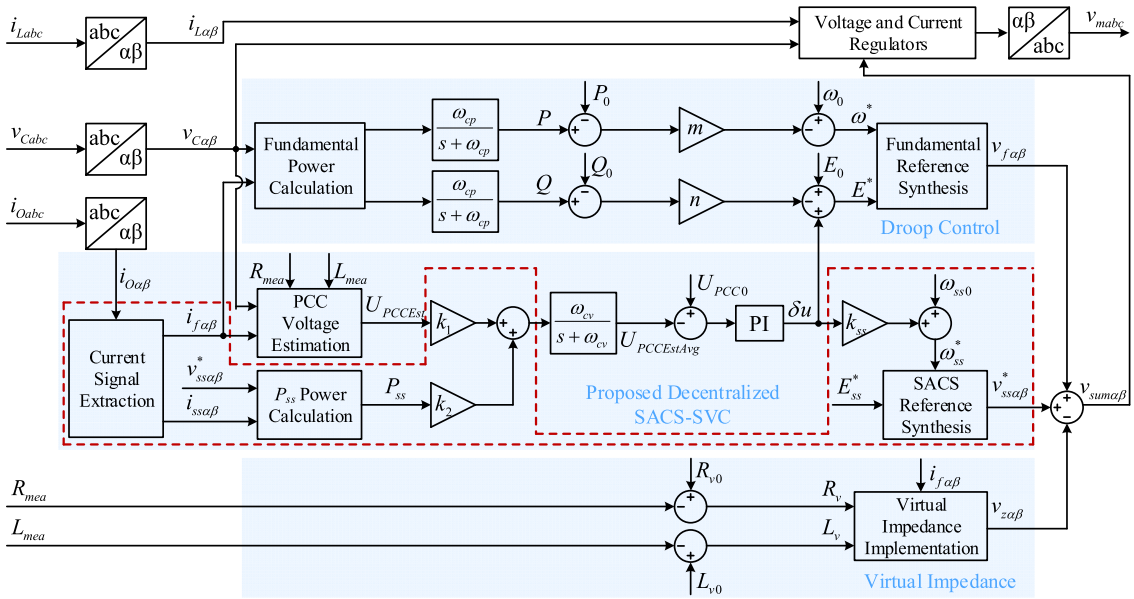

Fig. 4. Overall control block diagram of the local controller with the proposed SACS-SVC method, where elements inside the dashed box are added compared to existing PI-SVC.

as the estimation of the PCC voltage. It is worth noting that the input of the PI regulator in DG_2 is negative while the input of the PI regulator in DG_1 is positive after $t = t_2$. Therefore, because of the difference between the two $U_{\mathrm{PCC}\,Est}$ values, the value of δu in DG_2 will decrease while the value of δu in DG_1 will increase without limit. Finally, reactive power divergence will occur and the system will fail in the end.

III. Proposed SACS-Injection-Based SVC Method

A. Overall Control Scheme

The overall control scheme is shown in Fig. 4. The primary control is the same as that in PI-SVC. In the secondary control layer, the SACS control loop is added to the PI-SVC. The input of the PI regulator, which represents the average of estimated PCC voltage ($U_{\mathrm{PCC}\,EstAvg}$), is synthesized by using the estimated PCC voltage and the SACS active power multiplied by a pair of weight coefficients as follows:

$$U_{\mathrm{PCC}EstAvg} = k_1 U_{\mathrm{PCC}Est} + k_2 P_{ss} \tag{5}$$

where $U_{\mathrm{PCC}\,Est}$ is the estimated PCC voltage, P_{ss} is the SACS active power, and k_1 and k_2 are the weight coefficients, which are used to adjust the operation point in steady state.

Similar to (2) in PI-SVC, the average of the estimated PCC voltage $U_{\mathrm{PCC}\,EstAvg}$ is used for the PI regulator to generate the voltage compensation value δu as follows:

$$\delta u = \left(k_p s + \frac{k_i}{s}\right)\left(U_{\mathrm{PCC0}} - \frac{\omega_{cv}}{s+\omega_{cv}} U_{\mathrm{PCC}EstAvg}\right). \tag{6}$$

Moreover, a positive droop relation is built between the SACS frequency and the voltage compensation value as follows:

$$\omega_{ss}^{*} = \omega_{ss0} + k_{ss}\delta u \tag{7}$$

where ω_{ss}^{*} is the generated reference of the SACS angular frequency, ω_{ss0} is the nominal SACS angular frequency, and k_{ss} is the SACS droop coefficient.

Additionally, the SACS current is separated from the fundamental current by the signal extraction block to calculate the SACS active power. The fundamental power and the SACS active power are calculated as follows:

$$P = \frac{3}{2}\frac{\omega_{cp}}{s+\omega_{cp}}\left(v_{C\alpha}i_{f\alpha} + v_{C\beta}i_{f\beta}\right) \tag{8}$$

$$Q = \frac{3}{2}\frac{\omega_{cp}}{s+\omega_{cp}}\left(v_{C\beta}i_{f\alpha} - v_{C\alpha}i_{f\beta}\right) \tag{9}$$

$$P_{ss} = \frac{3}{2}\left(v_{ss\alpha}^{*}i_{ss\alpha} + v_{ss\beta}^{*}i_{ss\beta}\right) \tag{10}$$

where $i_{f\alpha}$ and $i_{f\beta}$ are the α-axis and β-axis components of the extracted fundamental current, respectively, $i_{ss\alpha}$ and $i_{ss\beta}$ are the α-axis and β-axis components of the extracted SACS current, respectively, $v_{ss\alpha}^{*}$ and $v_{ss\beta}^{*}$ are the α-axis and β-axis components of the SACS nominal voltage, respectively, and ω_{cp} is the cutoff angular frequency of the low-pass filter used in power calculation.

Note that, the low-pass filter used in voltage estimation in (2) and (6) is used to attenuate estimated voltage ripples and avoid interaction with the primary control loop, so that its cutoff angular frequency ω_{cv} is lower than the cutoff angular frequency ω_{cp} of the low-pass filter in power calculation in (8) and (9). Meanwhile, compared with (8) and (9), the low-pass filter in (10) is omitted because the weighted sum of P_{ss} and $U_{\mathrm{PCC}\,Est}$ will be filtered in (6).

Finally, with the SACS frequency reference derived in (7) and a constant amplitude E_{ss}^{*}, the SACS reference voltage can be expressed in $\alpha\beta$ frame as follows:

$$v_{ss\alpha}^{*} = E_{ss}^{*}\cos\left(\int \omega_{ss}^{*}dt\right) \tag{11}$$

$$v_{ss\beta}^{*} = E_{ss}^{*}\sin\left(\int \omega_{ss}^{*}dt\right). \tag{12}$$

B. Operation Principle

To gain a better understanding of the proposed method, the principle of active power sharing with P–ω droop control is reviewed here. In a microgrid with parallel DGs under inductive feeder impedance conditions, there is a positive correlation between the frequency and the output active power, thus, a negative droop control is built to form a closed loop with negative feedback. Because the frequency of each DG can synchronize with each other in steady state, the same active power can be guaranteed in P–ω droop control.

Similarly, the voltage compensation value can also be shared if we build a droop relation with a SACS frequency based on (7) when synchronized in steady state. However, the control loop is not yet closed and the estimated PCC voltage also needs to be taken into consideration.

As mentioned in Section II-B, inaccurate feeder impedance results in differences in the estimated PCC voltage in each DG, leading to a divergence of voltage compensation value and reactive power. To handle this issue, the difference in the estimated PCC voltage in each DG must be eliminated. Therefore, in the proposed method, the input of the PI regulator is replaced with the average of the estimated PCC voltage $U_{\mathrm{PCC}\,EstAvg}$, which is composed of the estimated PCC voltage and the SACS active power multiplied by a pair of weight coefficients as (5). It is worth noting that the correlation between the SACS power and the voltage compensation value is negative, thus, the SACS droop coefficient in (7) must be positive to form a closed loop with negative feedback so that the SACS active power can be tuned adaptively to eliminate the difference in the estimated PCC voltage in each DG.

Here, we take an example of two parallel DGs to explain the operation principle of the proposed method. To explain the synchronization process of the proposed method, it is assumed that $U_{\mathrm{PCC}\,Est2}$ is larger than $U_{\mathrm{PCC}\,Est1}$ due to inaccurate feeder impedance at the beginning, so δu_1 will be larger than δu_2 based on the analysis in Section II-B. After the proposed method is activated, the SACS frequency ω_{ss1}^{*} should be larger than ω_{ss2}^{*} based on the proposed δu–ω_{ss} droop relation in (7). Then, the SACS phase angle of DG_1 increases, and DG_2 decreases.

Therefore, P_{ss1} increases and P_{ss2} decreases according to steady state active power flow with inductive feeder impedance. Subsequently, $U_{\mathrm{PCC}\,EstAvg1}$ increases and $U_{\mathrm{PCC}\,EstAvg2}$ decreases according to (5), so that δu_1 decreases and δu_2 increases according to (6). This negative feedback loop adaptively adjusts P_{ss} and $U_{\mathrm{PCC}\,EstAvg}$ in each DG and guarantees the voltage compensation value δu to be equal in each DG unit because the injected SACS of each DG unit would synchronize to the same frequency in steady state. Therefore, the divergence issue can be solved.

Moreover, the proposed method is still valid even if there are much more DGs in the microgrid. This is because the SACS frequency can synchronize with each other in steady state, regardless of how many DGs there are in the microgrid, as shown in Fig. 5. Therefore, the same voltage compensation value δu can be guaranteed according to (7).

C. Current Signal Extraction

To calculate the fundamental power and the SACS active power, a signal extraction method, based on the second-order generalized integrator (SOGI), is utilized to separate the SACS current from the fundamental current, which contains two dual SOGI quadrature signal generators (DSOGI-QSGs) operating in parallel to separate the current at different frequencies, as shown in Fig. 6(a). Each DSOGI-QSG consists of two SOGI-QSGs working at the α-axis and β-axis, respectively, as shown in Fig. 6(b). The transfer function of each SOGI-QSG from the input signal v to the output signal v' is shown as

$$D(s) = \frac{v'}{v}(s) = \frac{k\omega s}{s^2 + k\omega s + \omega^2}. \tag{13}$$

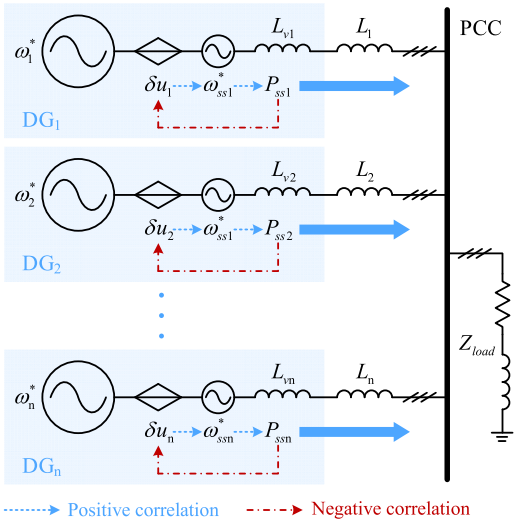

Fig. 5. Basic principle of the proposed SACS-SVC scheme in an islanded microgrid with multiple parallel DGs, where the correlations of variables are marked in different colors.

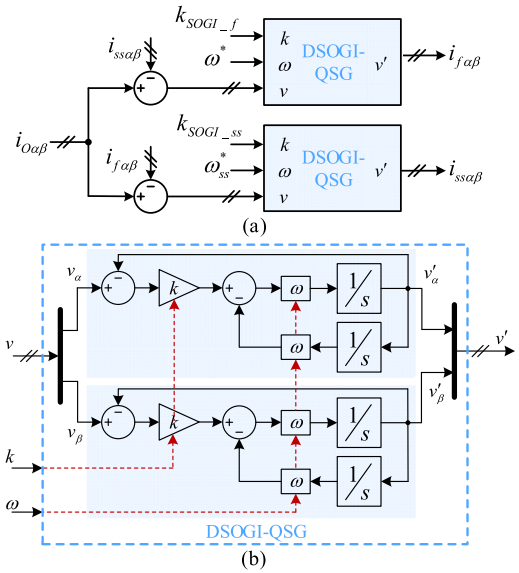

Fig. 6. Block diagram of (a) SOGI-based current signal extraction used in the proposed method and (b) DSOGI-QSG.

Each SOGI-QSG behaves as a band-pass filter at the resonant frequency. The bandwidth of SOGI-QSG is determined by the gain k. In the proposed method, $k_{\mathrm{SOGI\_}f}$ is set to $\sqrt{2}$ and $k_{\mathrm{SOGI\_}ss}$ is set to $\sqrt{2}/4$, respectively, according to [30]. Compared with the other SOGI-based algorithm, this method has advantages in terms of dynamic response and accuracy. The operational principle will not be introduced here because it is beyond the scope of this article.

D. Virtual Impedance Implementation

To improve the reactive power sharing performances based on the known feeder impedance, the virtual impedance method

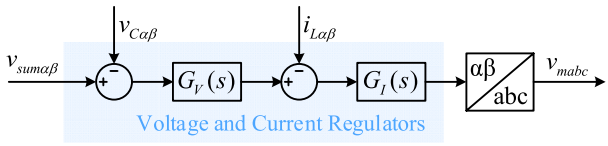

Fig. 7. Detailed block diagram of the voltage and current regulators block, which contains an outer voltage loop with a proportional-resonant controller and an inner current loop with a proportional controller.

[31] is adopted. The virtual voltage drop is calculated as follows:

$$\begin{bmatrix} R_v \\ L_v \end{bmatrix} = \begin{bmatrix} R_{v0} - R_{mea} \\ L_{v0} - L_{mea} \end{bmatrix} \tag{14}$$

$$\begin{bmatrix} v_{z\alpha} \\ v_{z\beta} \end{bmatrix} = \begin{bmatrix} R_v & -\omega_0 L_v \\ \omega_0 L_v & R_v \end{bmatrix} \begin{bmatrix} i_{f\alpha} \\ i_{f\beta} \end{bmatrix} \tag{15}$$

where R_{v0} and L_{v0} are the nominal equivalent feeder resistor and inductance, respectively.

E. Voltage and Current Regulators

To achieve precise voltage tracking, a dual-loop control structure is adopted, as shown in Fig. 7. The outer loop is a capacitor voltage control loop with a proportional-resonant controller, while the inner loop is an inductor current control loop with a proportional controller [32]. They are expressed as follows:

$$G_V(s) = k_{pV} + \frac{2k_{if}\omega_c s}{s^2 + 2\omega_c s + (\omega^*)^2} + \frac{2k_{iss}\omega_c s}{s^2 + 2\omega_c s + (\omega_{ss}^*)^2} \tag{16}$$

$$G_I(s) = k_{pI} \tag{17}$$

where k_{pV} is the proportional gain of the voltage controller, k_{if} and k_{iss} are the gains of the fundamental and SACS resonant controllers, respectively, ω_c is the cutoff angular frequency of the resonant controllers, and k_{pI} is the gain of the current proportional controller.

IV. Modeling and Parameter Design

To further analyze the effect of inaccurate feeder impedance, a small-signal differential mode model of two parallel DGs in an islanded microgrid, as shown in Fig. 2, is built in this section. The small-signal model for conventional droop control and secondary voltage control is already well established in the literature [33], [34]. Therefore, the control parameters of the proposed SACS-SVC, such as weight coefficients k_1 and k_2 and the SACS droop coefficient k_{ss}, are discussed in this section.

A. Differential Mode Model Analysis With Inaccurate Feeder Impedance

As mentioned before, inaccurate feeder impedance will cause reactive power divergence with PI-SVC. Therefore, the small-signal differential mode model is built to analyze the stability of the system and to guide parameter design of the proposed SACS-SVC. Specifically, the difference in the estimated PCC voltage is selected as the input of the differential mode model, while the reactive power sharing error is selected as the output

of the differential mode model. The details will be introduced in the following.

1) Simplification of Estimated PCC Voltage With Inaccurate Feeder Impedance: According to Thevenin's theorem, the PCC voltage can be calculated precisely with accurate feeder impedance as follows:

$$\begin{bmatrix} u_{\mathrm{PCC}\alpha} \\ u_{\mathrm{PCC}\beta} \end{bmatrix} = \begin{bmatrix} v_{C\alpha} \\ v_{C\beta} \end{bmatrix} - \begin{bmatrix} R & -\omega_0 L \\ \omega_0 L & R \end{bmatrix} \begin{bmatrix} i_{O\alpha} \\ i_{O\beta} \end{bmatrix} \tag{18}$$

$$U_{\mathrm{PCC}} = \sqrt{{u_{\mathrm{PCC}\alpha}}^2 + {u_{\mathrm{PCC}\beta}}^2} \tag{19}$$

where $U_{\mathrm{PCC}\alpha}$ and $U_{\mathrm{PCC}\beta}$ are the α-axis and β-axis components of the PCC voltage, respectively, R and L are the real values of the feeder resistor and inductor, respectively, and U_{PCC} is the real PCC voltage.

However, in practical applications, the feeder impedance is obtained through measurement. Due to inevitable measurement error, the feeder impedance will be inaccurate, which can be expressed as

$$\begin{cases} R_{mea} = (1 + e_R)R \\ L_{mea} = (1 + e_L)L \end{cases} \tag{20}$$

where e_R and e_L are the measurement error ratios of the feeder resistor and inductor, respectively.

To analyze the effect of inaccurate feeder impedance on the estimated PCC voltage, we substitute (8), (9), (18), (19), and (20) into (3) and (4) and use the Taylor formula for simplification. The estimated PCC voltage can be simplified as

$$U_{\mathrm{PCC}Est} \approx U_{\mathrm{PCC}} - \frac{e_R RP + e_L \omega_0 LQ}{\mathrm{U_{PCC}}}. \tag{21}$$

2) Analysis of Estimated PCC Voltage Difference: For simplification, assume two parallel DGs are in an islanded microgrid, as shown in Fig. 2, with the same inductive feeder impedance as follows:

$$\begin{cases} R_1 = R_2 = R \\ L_1 = L_2 = L \end{cases}. \tag{22}$$

Based on (22), the measured feeder impedance of each DG can be expressed as

$$\begin{cases} R_{mea1} = (1 + e_{R1})R \\ L_{mea1} = (1 + e_{L1})L \end{cases} \tag{23}$$

$$\begin{cases} R_{mea2} = (1 + e_{R2})R \\ L_{mea2} = (1 + e_{L2})L \end{cases} \tag{24}$$

where $e_{R\mathrm{n}}$ and $e_{L\mathrm{n}}$ are the measurement error ratios of the feeder resistor and inductor of the nth DG.

Hence, the difference in estimated PCC voltage (Δu_e) between two DGs can be calculated by substituting (23) and (24) into (21) as

$$\begin{aligned} \Delta u_e &= U_{\mathrm{PCC}Est1} - U_{\mathrm{PCC}Est2} \\ &\approx -\frac{R(e_{R1}P_1 + e_{R2}P_2) + \omega_0 L(e_{L1}Q_1 + e_{L2}Q_2)}{U_{\mathrm{PCC}}} \neq 0 \end{aligned} \tag{25}$$

where P_n and Q_n are the active and reactive powers of the nth DG, respectively.

It can be seen from (25) that Δu_e is not equal to zero. Therefore, Δu_e can be regarded as a nonzero disturbance to the control system. Additionally, the measurement error ratio of the feeder impedance is uncertain, however, the maximum measurement error can be determined as follows:

$$\begin{cases} 0 \le |e_{Rn}| \le e_{R\max} \\ 0 \le |e_{Ln}| \le e_{L\max} \end{cases}. \tag{26}$$

Assuming that $P_1 = P_2 = P_0$, and $Q_1 = Q_2 = Q_0$, the maximum value of Δu_e can be calculated as

$$\Delta u_{e\max} = \frac{2RP_0 e_{R\max} + 2\omega_0 LQ_0 e_{L\max}}{U_{\mathrm{PCC}}}. \tag{27}$$

3) Design of the Differential Mode Model: The small-signal linearization model is built by introducing a small perturbation around the equilibrium operation point, where the symbol "^" indicates the perturbation signal.

According to (1), the difference in the voltage amplitude reference with a small perturbation at the steady state operation point can be obtained as follows:

$$\hat{E}_1 = -n\hat{Q}_1 + \delta\hat{u}_1 \tag{28}$$

$$\hat{E}_2 = -n\hat{Q}_2 + \delta\hat{u}_2 \tag{29}$$

$$\begin{aligned} \Delta\hat{E} = \hat{E}_1 - \hat{E}_2 &= -n\left(\hat{Q}_1 - \hat{Q}_2\right) + (\delta\hat{u}_1 - \delta\hat{u}_2) \\ &= -n\Delta\hat{Q} + \Delta\delta\hat{u}. \end{aligned} \tag{30}$$

It can be seen from (30) that the perturbation consists of two parts: 1) the reactive power sharing error and 2) the voltage compensation value difference. The small-signal linearization model of the abovementioned two parts will be derived next.

On one hand, because of the assumption that the feeder impedances are the same in (23) and (24), the voltage amplitude E and the reactive power Q of two DGs can be regarded as the same in steady state. Therefore, the perturbation of the reactive power sharing error can be obtained as follows:

$$\Delta\hat{Q} = \hat{Q}_1 - \hat{Q}_2 = \frac{2E - U_{\mathrm{PCC}}}{X}(\hat{E}_1 - \hat{E}_2) = \frac{2E - U_{\mathrm{PCC}}}{X}\Delta\hat{E} \tag{31}$$

where X is the reactance of the feeder impedance.

On the other hand, the small perturbations of the estimated PCC voltage lead to the voltage compensation value differences between DG_1 and DG_2 based on (2). The equations can be derived as

$$\begin{aligned} \Delta\delta\hat{u} = \delta\hat{u}_1 - \delta\hat{u}_2 &= -\left(k_p s + \frac{k_i}{s}\right)\left(\hat{U}_{\mathrm{PCC}Est1} - \hat{U}_{\mathrm{PCC}Est2}\right) \\ &= -\left(k_p s + \frac{k_i}{s}\right)\Delta\hat{u}_e. \end{aligned} \tag{32}$$

Finally, the small-signal differential mode model of two DGs with PI-SVC is illustrated in Fig. 8, where ΔE_0 and ΔQ_0 are the input control signal and Δu_e is the input disturbance signal. The transfer function from input disturbance Δu_e to the reactive

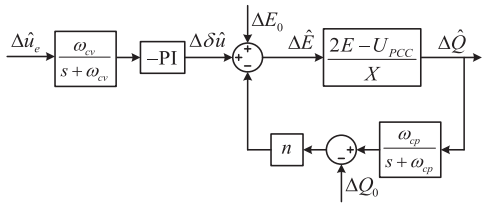

Fig. 8. Small-signal differential mode model of the islanded microgrid with PI-SVC.

power sharing error ΔQ can be derived as

$$G(s) = \frac{\Delta\hat{Q}}{\Delta\hat{u}_e} = \frac{As^2 + Bs + C}{s^3 + Ds^2 + Es} \tag{33}$$

where

$$\begin{aligned} A &= -k_p\omega_{cv}(2E - U_{\text{PCC}})/X \\ B &= -\omega_{cv}(\omega_{cp}k_p + k_i)(2E - U_{\text{PCC}})/X \\ C &= -k_i\omega_{cp}\omega_{cv}(2E - U_{\text{PCC}})/X \\ D &= \omega_{cp} + \omega_{cv} + n\omega_{cp}(2E - U_{\text{PCC}})/X \\ E &= \omega_{cp}\omega_{cv} + n\omega_{cp}(2E - U_{\text{PCC}})/X. \end{aligned}$$

According to (25) and (33), the nonzero Δu_e will be amplified by the PI regulator, leading to reactive power divergence, and the system will be unstable.

B. SACS Frequency and Amplitude Design

The injected SACS is an additional voltage component compared with the fundamental frequency. Thus, the frequency and the amplitude of the SACS must be carefully chosen according to the difficulty to extract the SACS and the power quality limitations.

1) Design of the SACS Frequency: To precisely separate the SACS component from the fundamental component, the frequency of the SACS must be carefully chosen. The following aspects should be taken into consideration when selecting the optimal SACS frequency.

First, the selected SACS frequency should avoid preexisting harmonics in the system, which maybe affect the extraction accuracy. For example, the low-order odd harmonic may exist in the system because of modulation or nonlinear loads. Second, the frequency of interharmonics or subharmonics should be avoided because the limitations for these frequencies are rigorous in the system. Third, the SACS frequency cannot be set too high because of the bandwidth of voltage control loop and the cutoff frequency of the output *LC* filter. Last but not least, the SACS frequency cannot be too close to the fundamental frequency in order to accurately separate SACS from the fundamental component. Therefore, the SACS frequency is set as four times of the fundamental frequency, which is 200 Hz in this article.

2) Design of the SACS Amplitude: The selection of the SACS amplitude is a tradeoff between the difficulty in extracting the SACS and the power quality limitations. On one hand, a large amplitude of SACS can reject noises apparently and ease signal extraction. However, the total harmonic distortion (THD) in microgrids is limited within 8%, and for individual harmonics within 5% according to IEEE standard 519 [35]. On the other hand, if the SACS amplitude is too small, the extraction accuracy will be affected by the sampling noise, analog-to-digital convert process, and signal extraction algorithm. Hence, the SACS amplitude is set as 0.5%–2% of the fundamental voltage amplitude, which will not exceed the THD limitations and can be easily extracted.

C. Design of Weight Coefficients k_1 and k_2

To design proper weight coefficients, the steady state operation point must be analyzed. In steady state, the SACS frequencies will synchronize with each other, and δu can be guaranteed to be the same for each DG according to (7). Meanwhile, δu being constant in steady state means that the input of the PI regulator is zero, namely $U_{\text{PCC}\,EstAvg}$ of each DG equals to the nominal PCC voltage. Therefore, the following equation can be derived:

$$k_1U_{\text{PCC}Est1} + k_2P_{ss1} = k_1U_{\text{PCC}Est2} + k_2P_{ss2} = U_{\text{PCC0}}. \tag{34}$$

Then, the difference in the SACS active power between DG_1 and DG_2 can be represented as

$$P_{ss1} - P_{ss2} = \frac{k_1}{k_2}(U_{\text{PCC}Est2} - U_{\text{PCC}Est1}) = -\frac{k_1}{k_2}\Delta u_e. \tag{35}$$

The total SACS active power can be regarded as constant if the load is unchanged as follows:

$$P_{ss1} + P_{ss2} = P_{ssL}. \tag{36}$$

By combining (35) and (36), the SACS active power of each DG can be represented as

$$P_{ss1} = \frac{P_{ssL}}{2} - \frac{k_1}{2k_2}\Delta u_e \tag{37}$$

$$P_{ss2} = \frac{P_{ssL}}{2} + \frac{k_1}{2k_2}\Delta u_e. \tag{38}$$

It can be seen from (37) and (38) that the SACS active power is related to the difference in the estimated PCC voltage and the weight coefficients k_1 and k_2. Hence, to guarantee the stability of the SACS, the weight coefficients should be carefully designed.

Here, we take DG_1 as an example to design the proper weight coefficients. Based on the steady state power flow with the inductive feeder impedance at the SACS frequency, the SACS active power of DG_1 can be expressed as

$$P_{ss1} = \frac{E_{ss}U_{ss}}{X_{ss1}}\sin\delta_{ss1} \approx \frac{E_{ss}^{*\,2}}{X_{ss1}}\delta_{ss1} \tag{39}$$

where U_{ss} is the SACS voltage at the PCC, which can be assumed to be equal to E_{ss}^* for simplification, δ_{ss} is the phase angle of DG_1 at the SACS frequency, and X_{ss1} is the feeder reactance of DG_1 at the SACS frequency.

The variation of the SACS active power with phase angle is depicted in Fig. 9. The active power varies as a sinusoidal wave of the angle, exhibiting a highly nonlinear relationship. When the angle is smaller than 90°, e.g., point a, the active power increases along with the angle; however, a further increase in the angle results in a reduction in active power when the phase angle

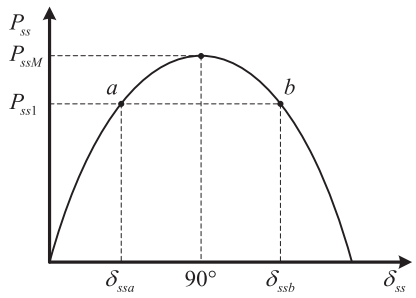

Fig. 9. Variation of active power with phase angle in each DG unit at the frequency of the injected SACS.

exceeds 90°, e.g., point b. According to the power angle stability criteria in power systems, a necessary condition for ensuring all the DGs remain synchronous and operate stably is to keep the angle below 90°. To evaluate the degree of angle stability, the stability reservation coefficient K_P is defined as follows:

$$K_P = \frac{P_{ssM} - P_{ss1}}{P_{ss1}} \times 100\% \tag{40}$$

where P_{ssM} is the maximum transferred power when δ_{ss} equals to 90°. An increase in K_P results in a larger angle stability margin, whereas the transferred power will decline. In power system design guides [36], K_P is recommended to be within 15% to 20% to retain a sufficient stability margin. However, different from a power system, the principal function of the SACS is to establish a link among DGs instead of transferring power; therefore, K_P should be designed to be larger than in a power system to guarantee a sufficient stability margin of the SACS. Based on this phenomenon, a K_P larger than 40% is recommended in this control method. The upper limit for the SACS real power can be obtained as

$$P_{ss1} \le \frac{P_{ssM}}{1.4}. \tag{41}$$

By substituting (27) and (37) into (41), the minimum value for weight coefficient can be determined as follows:

$$\frac{k_1}{k_2} \ge \frac{0.7P_{ssL}X_{ss1} - {E^*_{ss}}^2}{0.7X_{ss1}\Delta u_{e\max}}. \tag{42}$$

Moreover, assuming that the PCC voltage is fully restored to the nominal voltage, e.g., $U_{\rm PCC} = U_{\rm PCC0}$, and substituting (21) and (26) into (34), the steady state relationship between k_1 and k_2 can be derived as

$$k_1 \approx \frac{U_{\rm PCC0} - k_2 P_{ss1}}{U_{\rm PCC0} - \frac{e_{R\max}RP_0 + e_{L\max}\omega_0 LQ_0}{U_{\rm PCC0}}}. \tag{43}$$

D. Design of the SACS Droop Coefficient K_{ss}

In this section, the small-signal differential mode model will be further perfected based on the proposed SACS-SVC to analyze the dynamic stability and design of the SACS droop coefficient.

Based on (5), the small perturbations of the average of estimated PCC voltage and the difference between DG_1 and DG_2 can be derived as

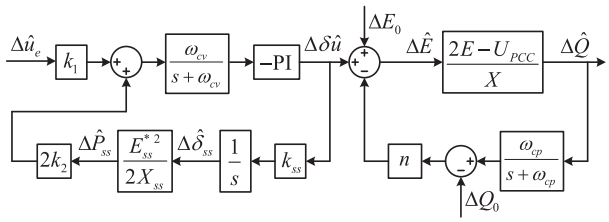

Fig. 10. Small-signal differential mode model of the islanded microgrid with the proposed SACS-SVC.

$$\hat{U}_{\rm PCC}{}_{EstAvg1} = k_1\hat{U}_{\rm PCC}{}_{Est1} + k_2\hat{P}_{ss1} \tag{44}$$

$$\hat{U}_{\rm PCC}{}_{EstAvg2} = k_1\hat{U}_{\rm PCC}{}_{Est2} + k_2\hat{P}_{ss2} \tag{45}$$

$$\begin{aligned}\Delta\hat{U}_{\rm PCC}{}_{EstAvg} &= \hat{U}_{\rm PCC}{}_{EstAvg1} - \hat{U}_{\rm PCC}{}_{EstAvg1} \\ &= k_1(\hat{U}_{\rm PCC}{}_{Est1} - \hat{U}_{\rm PCC}{}_{Est2}) + k_2(\hat{P}_{ss1} - \hat{P}_{ss2}) \\ &= k_1\Delta\hat{u}_e + k_2\Delta\hat{P}_{ss}.\end{aligned} \tag{46}$$

Next, the voltage compensation value difference with small perturbations can be derived as

$$\begin{aligned}\Delta\delta\hat{u} = \delta\hat{u}_1 - \delta\hat{u}_2 &= -\left(k_p s + \frac{k_i}{s}\right)\left(\hat{U}_{\rm PCC}{}_{EstAvg1} - \hat{U}_{\rm PCC}{}_{EstAvg2}\right) \\ &= -\left(k_p s + \frac{k_i}{s}\right)\left(k_1\Delta\hat{u}_e + k_2\Delta\hat{P}_{ss}\right).\end{aligned} \tag{47}$$

Then, assuming a small perturbation of the voltage compensation value is introduced at the steady state operation point in (7), the following equations can be obtained:

$$\hat{\omega}_{ss1} = k_{ss}\delta\hat{u}_1 \tag{48}$$

$$\hat{\omega}_{ss2} = k_{ss}\delta\hat{u}_2 \tag{49}$$

$$\Delta\hat{\omega}_{ss} = \hat{\omega}_{ss1} - \hat{\omega}_{ss2} = k_{ss}(\delta\hat{u}_1 - \delta\hat{u}_2) = k_{ss}\Delta\delta\hat{u}. \tag{50}$$

The difference in the SACS frequency leads to the phase angle difference between DG_1 and DG_2 as follows:

$$\Delta\hat{\delta}_{ss} = \hat{\delta}_{ss1} - \hat{\delta}_{ss2} = \frac{\Delta\hat{\omega}_{ss}}{s} = \frac{k_{ss}}{s}\Delta\delta\hat{u}. \tag{51}$$

Because the total SACS active power is assumed to be constant when loads are unchanged, which is independent of phase angle perturbation, the SACS active power perturbation only flows between DGs. Thus, based on (22) and (39), the SACS active power perturbations of DG_1 and DG_2 have the following relation:

$$\hat{P}_{ss1} = -\hat{P}_{ss2} = \frac{E_{ss}U_{ss}}{X_{ss1} + X_{ss2}}\sin\Delta\hat{\delta}_{ss} \approx \frac{{E^*_{ss}}^2}{2X_{ss}}\Delta\hat{\delta}_{ss}. \tag{52}$$

Therefore, the perturbation of the SACS active power difference can be calculated as follows:

$$\Delta\hat{P}_{ss} = \hat{P}_{ss1} - \hat{P}_{ss2} = \frac{{E^*_{ss}}^2}{X_{ss}}\Delta\hat{\delta}_{ss}. \tag{53}$$

Finally, the small-signal differential mode model of two DGs with SACS-SVC is illustrated in Fig. 10. Note that the dynamic

TABLE I
SIMULATION AND EXPERIMENTAL PARAMETERS

Symbol	Description		Value	
			Simulation	Experiment
R_n+L_n	Feeder impedance of DG$_n$ (Ω+mH)	DG$_1$	0.01+4	1+4
		DG$_2$	0.01+4	1+3
		DG$_3$		1+4
R_{mean} +L_{mean}	Measured feeder impedance of DG$_n$ (Ω+mH)	DG$_1$	0.01+4.04	0.9+3.8
		DG$_2$	0.01+3.96	0.8+3.2
		DG$_3$		0.9+3.9
R_{v0} +L_{v0}	Nominal virtual feeder impedance (Ω+mH)	DG$_1$	0.01+4	1+4
		DG$_2$	0.01+4	1+4
		DG$_3$		1.3+5.3
m	P–ω droop coefficient (rad/s/W)		2×10^{-4}	7×10^{-5}
n	Q–E droop coefficient (V/var)		2×10^{-4}	10^{-2}
U_{PCC0}	Nominal PCC line voltage (V)		283	200
k_1	Weighting coefficient		0.968	0.978
k_2	Weighting coefficient		58.083	42.135
V_{dc}	DC voltage (V)		600	
f_s	Switching frequecy (kHz)		12.5	
L_f	Filter inductance (mH)		3	
C_f	Filter capacitance (μF)		30	
ω_{cp}	Cutoff angular frequency of the low-pass filter in power calculation (rad/s)		2π*10	
ω_{cv}	Cutoff angular frequency of the low-pass filter in voltage estimation (rad/s)		2π*5	
E^*_{ss}	SACS nominal voltage amplitude (V)		2	
ω_{ss0}	SACS nominal angular frequency (rad/s)		2π*200	
k_{ss}	SACS droop coefficient		0.01	
k_p	Proportional gain of PI regulator		1	
k_i	Integral gain of PI regulator		0.5	

characteristic of the signal extraction block and the inner loops, whose bandwidth is much higher than the cutoff frequency of the low-pass filters, as mentioned in Section II, are ignored.

Based on the small-signal differential mode model shown in Fig. 10, the transfer function from input disturbance Δu_e to the reactive power sharing error ΔQ can be derived as

$$G(s) = \frac{\Delta\hat{Q}}{\Delta\hat{u}_e} = \frac{A's^3 + B's^2 + C's}{s^4 + D's^3 + E's^2 + F's + G'} \tag{54}$$

where

$$\begin{aligned}
A' &= -k_1k_p\omega_{cv}(2E - U_{\text{PCC}})/X \\
B' &= -k_1\omega_{cv}(k_p\omega_{cp} + k_i)(2E - U_{\text{PCC}})/X \\
C' &= -k_1k_i\omega_{cp}\omega_{cv}(2E - U_{\text{PCC}})/X \\
D' &= (\omega_{cp} + n\omega_{cp}(2E - U_{\text{PCC}})/X) + \omega_{cv} \\
E' &= \omega_{cv}(\omega_{cp} + n\omega_{cp}(2E - U_{\text{PCC}})/X) + \omega_{cv}k_p \\
F' &= k_p\omega_{cv}(\omega_{cp} + n\omega_{cp}(2E - U_{\text{PCC}})/X) \\
&\quad + k_ik_2k_{ss}\omega_{cv}{E^*_{ss}}^2/X_{ss} \\
G' &= k_2k_ik_{ss}\omega_{cv}{E^*_{ss}}^2(\omega_{cp} + n\omega_{cp}(2E - U_{\text{PCC}})/X)/X_{ss}.
\end{aligned}$$

Next, according to the simulation parameters listed in Table I, the root locus of the transfer function is illustrated in Fig. 11.

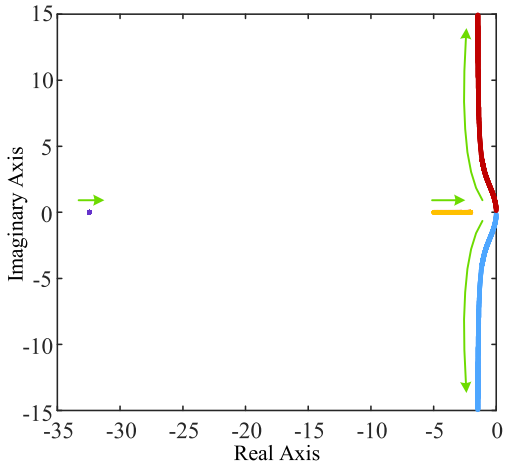

Fig. 11. Root locus of the transfer function of the small-signal differential mode model with respect to variation in the SACS droop coefficient k_{ss} from 0 to 0.5.

It can be seen that, when k_{ss} increases, the dominant conjugate eigenvalues move to the left-half plane with the increase of the imaginary part, leading to an increasingly fast but overdamped reactive power response. Therefore, considering the tradeoff between the settling time and the oscillation frequency of the reactive power response, k_{ss} should not be set too high.

Finally, the abovementioned model is built based on the assumption that the feeder impedance is the same. In most cases, mismatch of feeder impedance often occurs. Thus, the equivalent feeder impedance can be used during the parameter design process.

E. Effect of Background Harmonic at SACS Frequency

If the background harmonic at SACS frequency exists in the system, there will be an additional SACS active power caused by the background harmonic. Therefore, according to (34), the steady state operating point of PCC voltage with background harmonic can be represented as

$$U_{\text{PCC}} \approx U_{\text{PCC}Est} = \frac{U_{\text{PCC0}}}{k_1} - \frac{k_2}{k_1}(P_{ss} + P_{ssh}) \tag{55}$$

where P_{ssh} is the SACS active power caused by the background harmonic.

It can be seen from (55) that the steady state operating point of PCC voltage is related to the additional SACS active power caused by the background harmonic P_{ssh}. Therefore, the background harmonic at SACS frequency will affect the steady state operating point of PCC voltage.

In general, the background harmonic is caused by the nonlinear loads that inject harmonic current to generate harmonic voltage drop on the grid impedance. Therefore, a harmonic current source located at the PCC is used to emulate the background harmonic caused by the nonlinear loads.

Assuming the background harmonic current in $\alpha\beta$ frame can be expressed as

$$i_{h\alpha} = I_h\cos(\omega_h t + \theta_h) \tag{56}$$

$$i_{h\beta} = I_h \sin(\omega_h t + \theta_h) \tag{57}$$

where I_h is the amplitude of the background harmonic current, ω_h is the angular frequency of the background harmonic current, and θ_h is the phase angle difference between SACS nominal voltage and the background harmonic current.

Therefore, combing (11), (12), (56), and (57), the additional SACS active power caused by the background harmonic current can be calculated as

$$\begin{aligned} P_{ssh} &= \frac{3}{2}\left(v^*_{\alpha ss} i_{h\alpha} + v^*_{ss\beta} i_{h\beta}\right) \\ &= \frac{3}{2} E^*_{ss} I_h \cos\left[\left(\omega^*_{ss} - \omega_h\right) t - \theta_h\right]. \end{aligned} \tag{58}$$

It can be seen from (58) that the angular frequency difference between the background harmonic current and SACS nominal voltage will determine whether the P_{ssh} is constant or sinusoidal.

If the frequency of background harmonic current is the same with the SACS frequency, the additional SACS active power is constant, namely, this background harmonic current source can be considered as a negative resistor at SACS frequency that injected an additional SACS active power into the system. In this case, the background harmonic will cause an additional negative SACS active power P_{ssh}, therefore, the steady state operating point of the PCC voltage will increase.

If the frequency of background harmonic current is different from the SACS frequency, the additional SACS active power is a time-varying sinusoidal component. In this case, the background harmonic will cause the PCC voltage oscillate around the steady state operating point.

V. Simulation and Experimental Results

To verify the effectiveness of the proposed method, simulation and experimental results are given for the same topology based on a typical islanded microgrid with parallel DGs, as shown in Fig. 2. The detailed simulation and experimental parameters are listed in Table I. Because some of the variables are difficult to measure experimentally, the simulations are presented to verify the PCC voltage restoration performance and the parameter design methodology introduced in Section IV through the PSCAD/EMTDC platform. Meanwhile, the comparisons between the existing PI-SVC method and the proposed SACS-SVC method are conducted in the experiments.

A. Simulation Results

In the simulation, only the conventional droop control and virtual impedance were initially adopted, then the proposed SACS-SVC was implemented at $t = 2$ s. The detailed waveforms of some key variables in the proposed method will be given to gain a better understanding of its operational principle. Verifications of the small-signal differential mode model and the parameter design methodology introduced in Section IV will also be presented.

1) PCC Voltage Restoration Verification: At the beginning, only conventional *droop* control and virtual impedance were implemented. Because of the inaccurate feeder impedance, the estimated PCC voltages $U_{\mathrm{PCC}\,Est}$ of two DGs are slightly different from each other. The terminal voltage E and the reactive power Q are identical for both DGs because of the same equivalent feeder impedance. Afterward, the proposed method was implemented at $t = 2$ s. The input of the PI regulator was synthesized by using $U_{\mathrm{PCC}\,Est}$ and the SACS active power P_{ss} multiplied by a pair of weight coefficients to generate the voltage compensation value δu according to (5) and (6). Meanwhile, the positive droop relation was built between compensation value δu and the SACS angular frequency ω_{ss} according to (7). Detailed waveforms of the aforementioned variables are shown in Fig. 12. It can be seen that the difference of $U_{\mathrm{PCC}\,Est}$ is made up of the difference of P_{ss} to guarantee that $U_{\mathrm{PCC}\,EstAvg}$, which is used as the input signal of the PI regulator, is identical for the two DGs. Therefore, the effect of inaccurate feeder impedance in PI-SVC can be solved. Furthermore, the SACS frequencies can be synchronized with each other in steady state, so δu can also be shared according to (7), which will not deteriorate reactive power sharing performances after compensation. Finally, the PCC voltage can also be fully restored with the proposed method.

2) Transient Performance Investigation Under Feeder Impedance Change: To analysis the transient performance of the proposed method, the case that feeder impedance change during SACS- SVC were investigated. Because the feeder impedance was obtained through offline estimation rather than online estimation, the DG unit cannot update the feeder impedance information after system was started. Thus, when the feeder impedance was changed the DG unit would still use the designed feeder impedance to estimate PCC voltage. As shown in Fig. 13, the proposed method was implemented at $t = 2$ s and the feeder inductance changed at $t = 16$ s from 4 mH to 8 mH. It can be seen that when the feeder impedance changed, the system moved to another steady state operating point and the steady state voltage error between the nominal PCC voltage and the real PCC voltage also appeared, which means the estimated PCC voltage is no more equal to the real PCC voltage.

According to (21), there will be a voltage drop in the estimated PCC voltage after feeder impedance changed. In other word, there will be a voltage drop between the estimated PCC voltage and the real PCC voltage. Therefore, when secondary voltage control enters to a steady state, the estimated PCC voltage will be restored to its nominal value instead of the real PCC voltage and a steady state voltage error will occur due to the change in feeder impedance.

3) $\mathrm{K_{ss}}$ *Design Methodology Verification:* In this simulation case, the small-signal *differential* mode model and the k_{ss} design methodology were investigated. According to the trajectory of dominant conjugate eigenvalues based on the small-signal differential mode model, as shown in Fig. 14, k_{ss} was set to 0.022, 0.071, and 0.234, respectively. The simulation results for reactive power Q and reactive power sharing error ΔQ are shown in Fig. 15. Note that the real part of the conjugate eigenvalues with $k_{ss} = 0.071$ is twice bigger than that with $k_{ss} = 0.022$. Therefore, the settling time of ΔQ in Fig. 15(a) is nearly twice as long as that of in Fig. 15(b). However, the imaginary part of the conjugate eigenvalue with $k_{ss} = 0.071$ is half of that with $k_{ss} = 0.234$. Therefore, the oscillation frequency during the dynamic

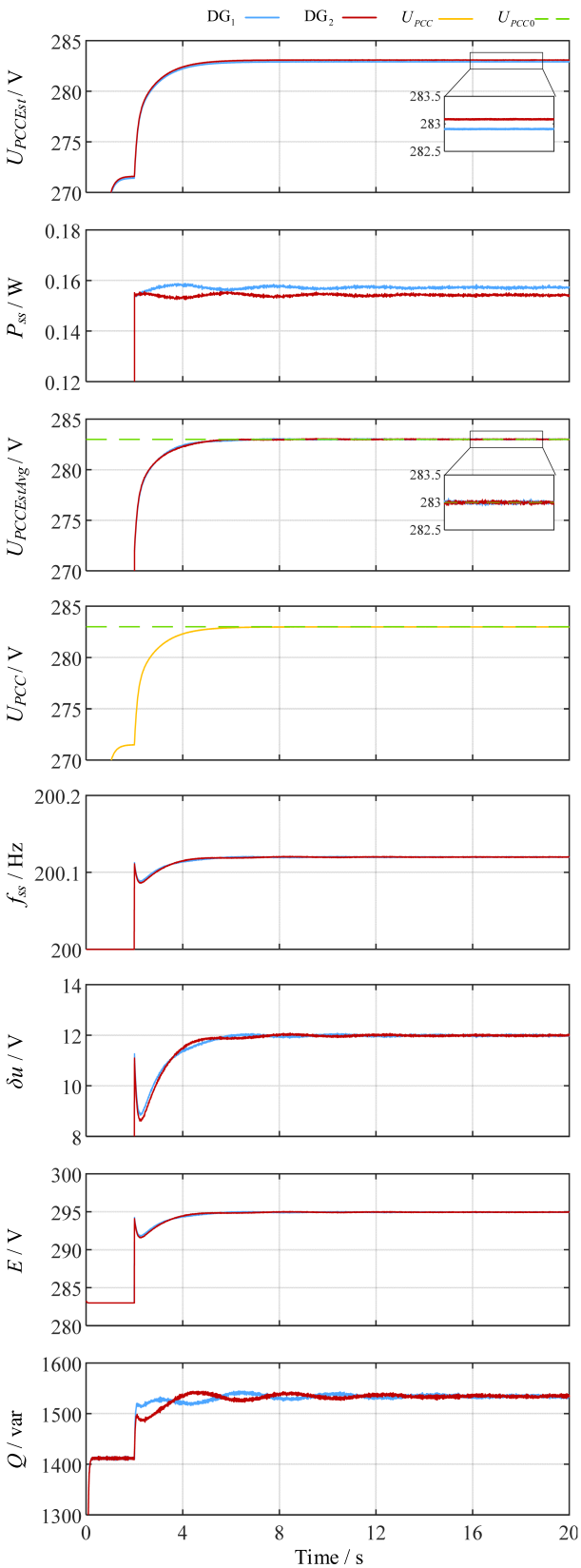

Fig. 12. Simulated waveforms of the estimated PCC voltage $U_{\mathrm{PCC}\,Est}$, SACS active power P_{ss}, the average of estimated PCC voltage $U_{\mathrm{PCC}\,EstAvg}$, PCC voltage U_{PCC}, SACS frequency f_{ss}, voltage compensation value δu, terminal voltage E, and reactive power Q of two DGs with the proposed SACS-SVC.

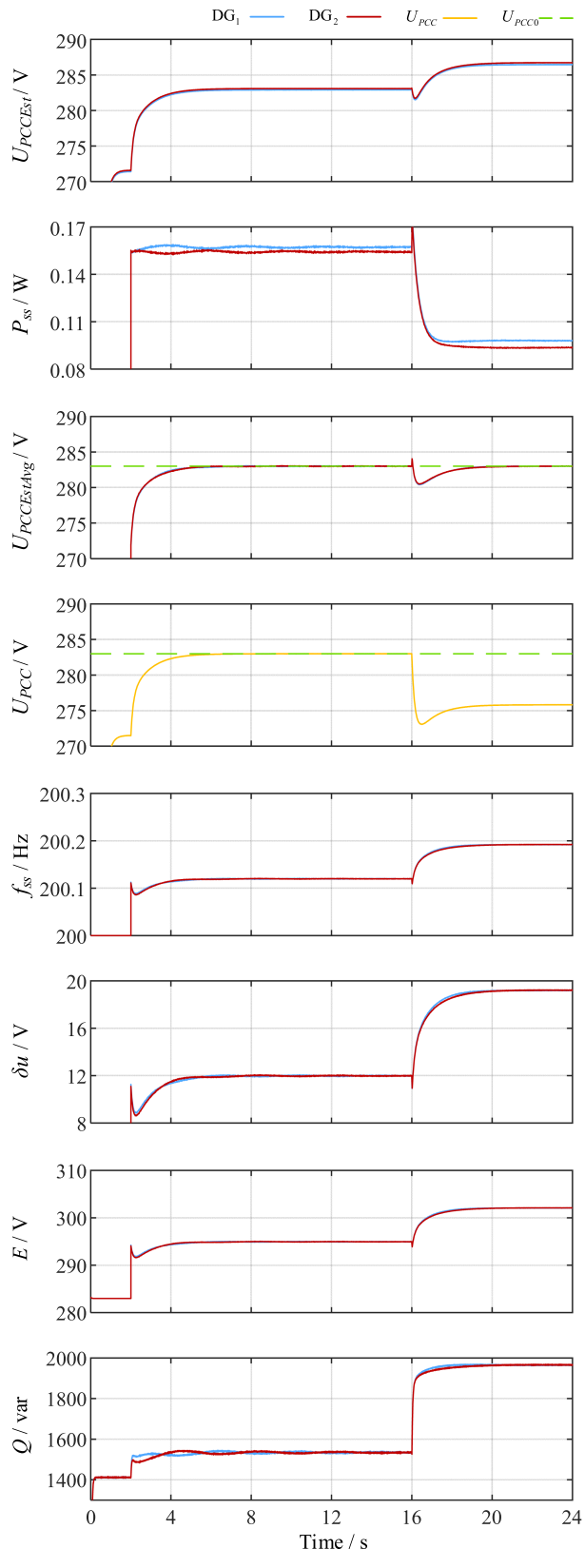

Fig. 13. Simulated waveforms of the estimated PCC voltage $U_{\mathrm{PCC}\,Est}$, SACS active power P_{ss}, the average of estimated PCC voltage $U_{\mathrm{PCC}\,EstAvg}$, PCC voltage U_{PCC}, SACS frequency f_{ss}, voltage compensation value δu, terminal voltage E, and reactive power Q of two DGs with the proposed SACS-SVC, when feeder inductance changed at t = 16 s from 4 mH to 8 mH.

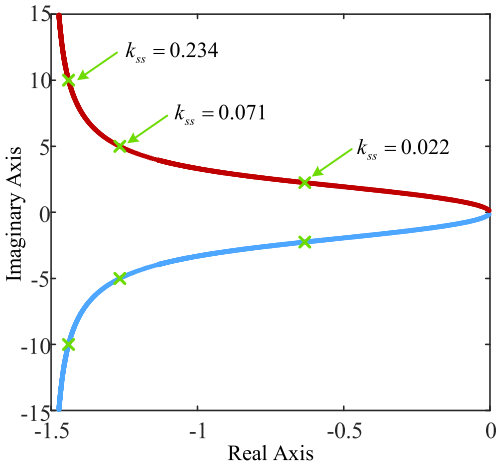

Fig. 14. Trajectory of dominant conjugate eigenvalues with respect to variation in the SACS droop coefficient k_{ss} from 0 to 0.5.

response of ΔQ in Fig. 15(c) is nearly twice higher than that in Fig. 15(b). It can be seen that, with the increase of k_{ss}, the settling time can be reduced, but the reactive power oscillation frequency will increase as well. Hence, the small-signal differential mode model and k_{ss} design methodology are proved.

4) Verification of Background Harmonic at SACS Frequency: In this simulation, a harmonic current source located at the PCC is used to emulate the background harmonic caused by the nonlinear loads. According to IEEE standard 519 [35], the amplitude of the harmonic current is chosen as 2% of the nominal current, which is 0.4 A in this simulation.

In Fig. 16(a), the background harmonic current frequency equals to the SACS frequency, therefore, the calculated SACS active power is reduced by a constant value and the steady state operating point of PCC voltage increase. In Fig. 16(b), the background harmonic current frequency, which is chosen four times of the fundamental frequency, is different from the SACS frequency, therefore, the calculated SACS active power and the PCC voltage oscillate around the steady state operating point.

B. Experimental Results

Hardware experiments were conducted based on an islanded microgrid with three parallel DGs, as shown in Fig. 17, and the detailed parameters are listed in Table I. A digital signal processor (Texas Instruments TMS320F28335) was used to realize the control algorithm. A power analyzer (Yokogawa WT1804E) was used to measure the output active and reactive power of the DGs. The power analyzer outputs the measured reactive power through an embedded DA converter, after which an oscilloscope (Tektronix DPO3014) is used to capture the waveforms of real reactive power. Another oscilloscope (Tektronix DPO4104B) was used to capture the waveforms of the PCC voltage and the voltage compensation value through the DA converter on the digital signal processor.

To verify the effectiveness of the proposed method comprehensively, two cases were investigated. In Case 1, the comparison of the proposed SACS-SVC and existing PI-SVC was demonstrated by considering different activation times of secondary control and inaccurate feeder impedance, respectively. Case 2 was used to demonstrate the robustness of the proposed control method against load disturbances and THD analysis before and after implementing the proposed control method.

Moreover, the virtual impedance was set according to capacity ratio of the three DGs, which is 1:1:0.75, to optimally share the reactive power among DGs. However, it is worth noting that the reactive power ratio is not strictly equal to 1:1:0.75 according to the experimental waveforms captured by the oscilloscope. This is because that the implemented virtual impedance is set based on the inaccurate feeder impedance.

1) Case 1: Proposed SACS-SVC Versus Existing PI-SVC: In this case, the performance of the proposed SACS-SVC was compared with that of the existing PI-SVC. The DG was initially controlled by conventional droop control with virtual impedance based on the known feeder impedance, then the secondary control was implemented at $t = 4$ s.

To demonstrate the effect of the activation delay of secondary control, the secondary controller in DG_2 was initiated with a 500 ms delay compared with the other two DGs. The simulation results are depicted in Figs. 18 and 19. As shown in Fig. 18, although the PCC voltage can be fully restored with the existing PI-SVC, reactive power sharing performances deteriorated because of the different voltage compensation values caused by the activation delay. However, as shown in Fig. 19, the PCC voltage can be fully restored and reactive power sharing performances can also be guaranteed regardless of activation delay with the proposed SACS-SVC.

To demonstrate the effect of inaccurate feeder impedance, inaccurate feeder impedance was used to estimate PCC voltage for both control methods. The experimental results are depicted in Figs. 20 and 21. It can be seen that inaccurate feeder impedance can cause reactive power divergence in PI-SVC, as explained in Section II-B, while the proposed SACS-SVC exhibits robustness against the disturbance in feeder impedance and guarantees the same reactive power sharing performances before and after voltage compensation.

2) Case 2: Robustness to Load Disturbance and THD Analysis: To demonstrate robustness to load changes, the voltage compensation value and PCC voltage response of the system to a step load change, as well as the corresponding reactive power of each DG, are illustrated in Fig. 22. Although the PCC voltage is not so precisely identical to 200 V, as a result of inaccurate feeder impedance, the PCC voltage regulation performance is still acceptable.

To confirm that the injected SACS does not affect voltage quality excessively, PCC voltage waveforms and the corresponding THD analysis results before and after injecting the SACS are depicted in Fig. 23. According to Fig. 23(a) and (b), the THD of the PCC voltage increases slightly from 0.89% to 1.17% after injecting the SACS. Meanwhile, as shown in Fig. 23(c), the fourth-order harmonic voltage, which is the SACS frequency, increases considerably but is still within a reasonable range and does not exceed the limitation mentioned in [37].

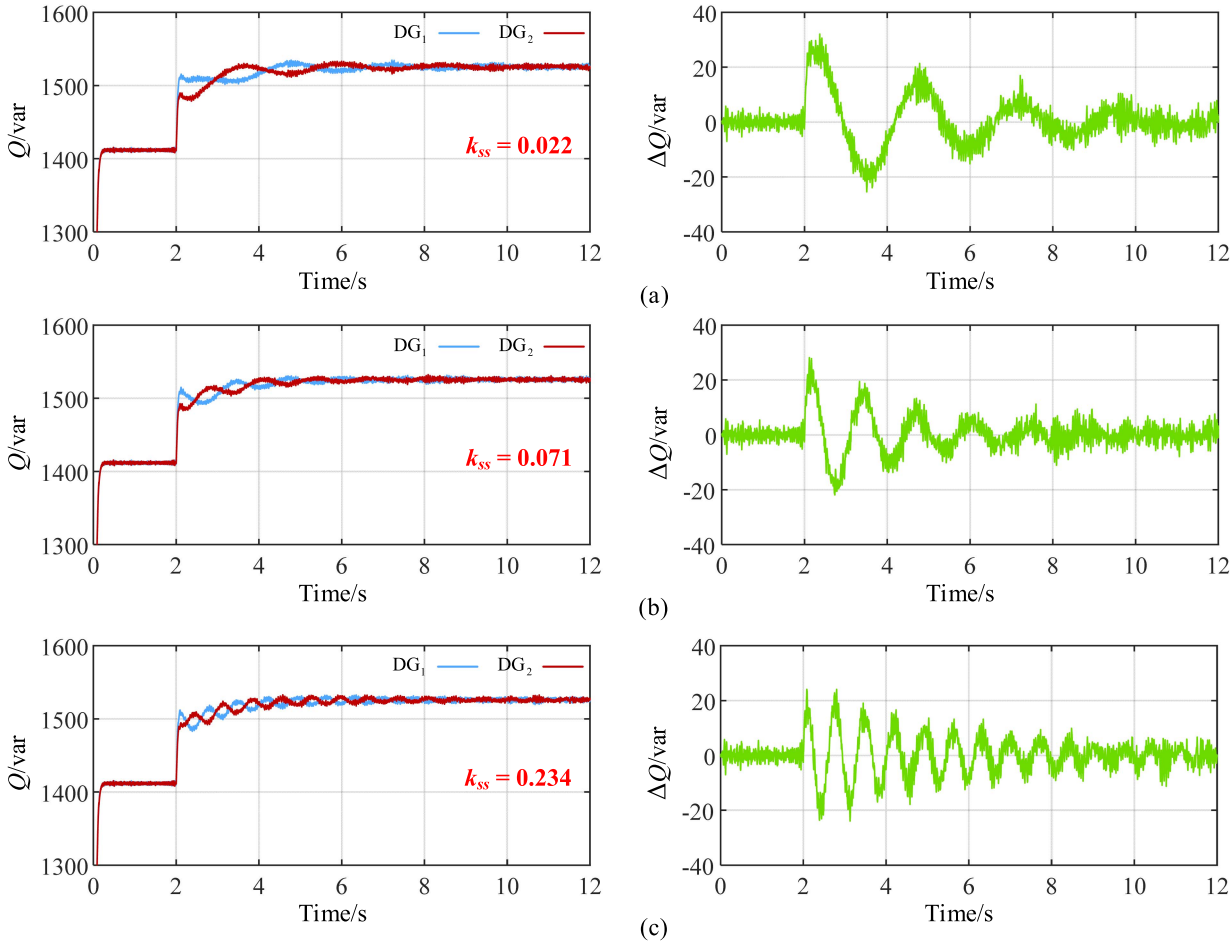

Fig. 15. Simulated waveforms of reactive power Q and reactive power sharing error ΔQ with different SACS droop coefficients: (a) $k_{ss} = 0.022$; (b) $k_{ss} = 0.071$; (c) $k_{ss} = 0.234$.

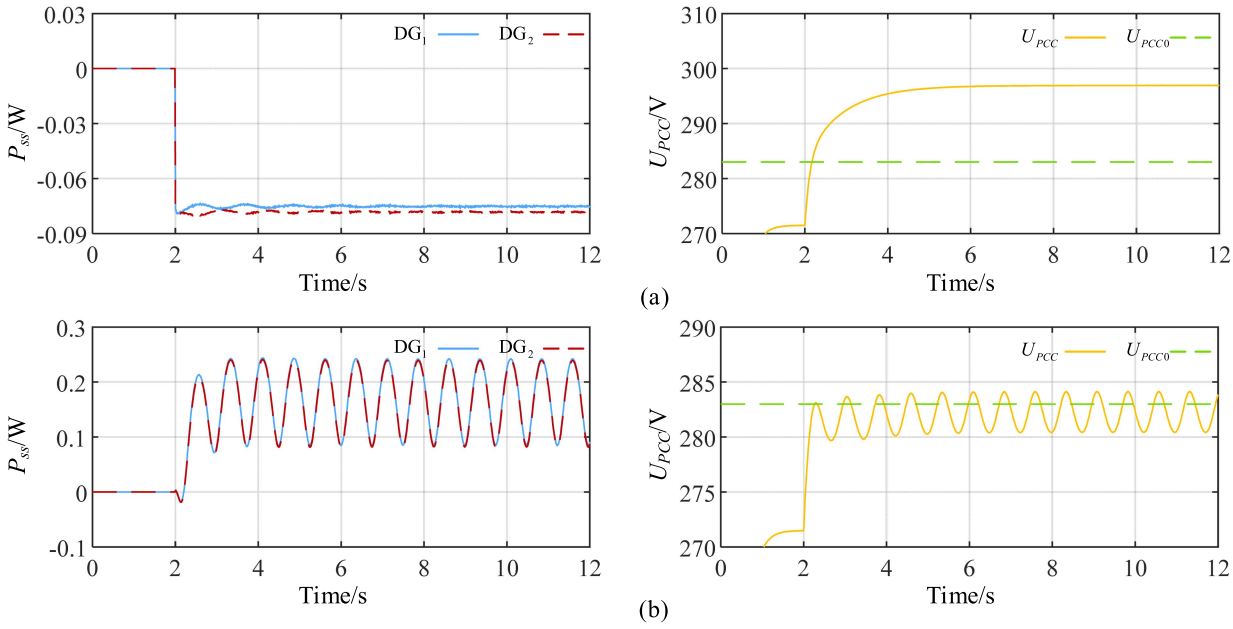

Fig. 16. Simulated waveforms of the SACS active power P_{ss} and PCC voltage U_{PCC} of two DGs with the proposed SACS-SVC with different background harmonic frequency. (a) Background harmonic frequency equals to the SACS frequency. (b) Background harmonic frequency is different from the SACS frequency.

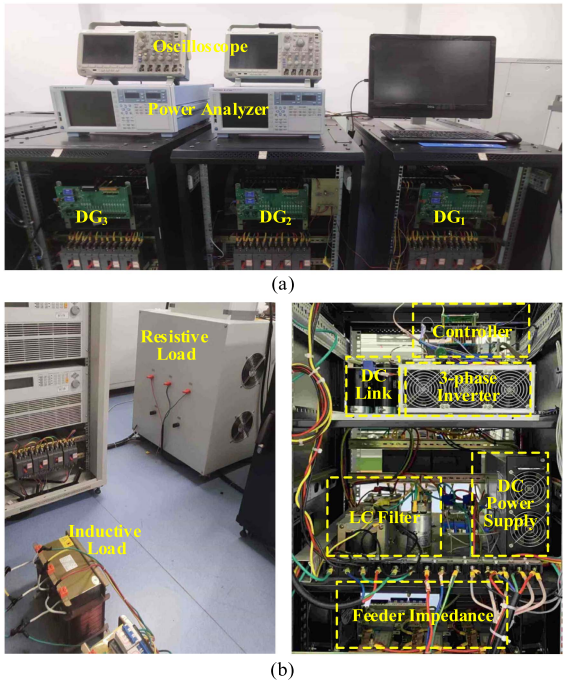

Fig. 17. Experimental setup for an islanded microgrid with parallel DGs. (a) System overall diagram. (b) Loads and structure inside each DG cabinet.

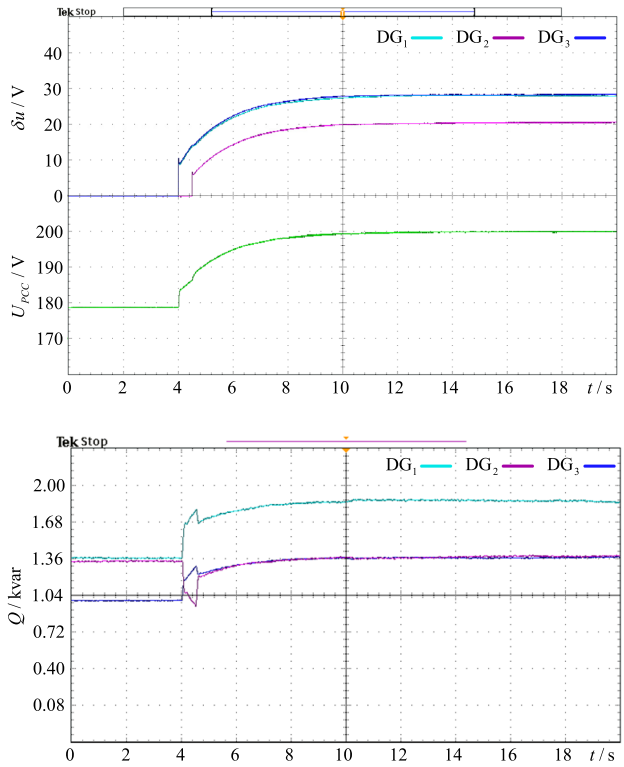

Fig. 18. Experimental waveforms of voltage compensation value δu, PCC voltage U_{PCC}, and reactive power Q of two DGs with 500 ms activation delay under PI-SVC.

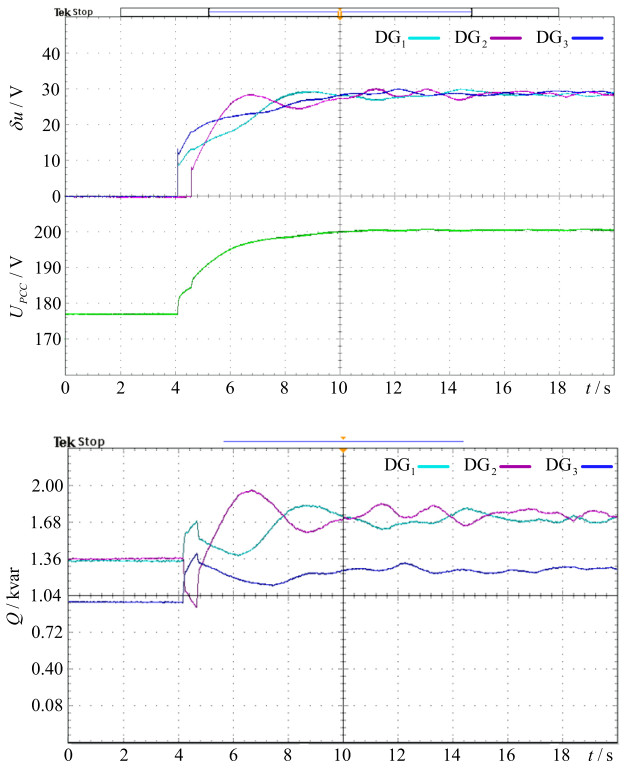

Fig. 19. Experimental waveforms of voltage compensation value δu, PCC voltage U_{PCC}, and reactive power Q of two DGs with 500 ms activation delay under the proposed SACS-SVC.

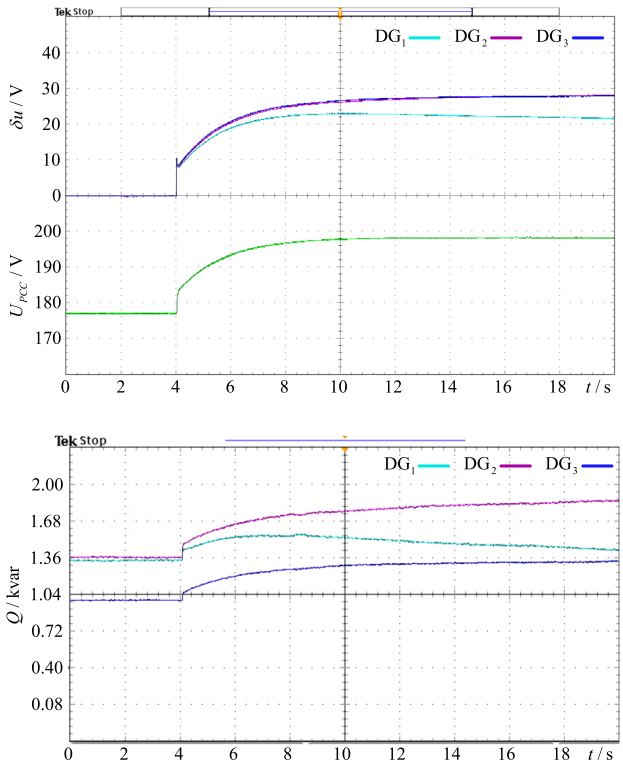

Fig. 20. Experimental waveforms of voltage compensation value δu, PCC voltage U_{PCC}, and reactive power Q of two DGs with inaccurate feeder impedance under the PI-SVC.

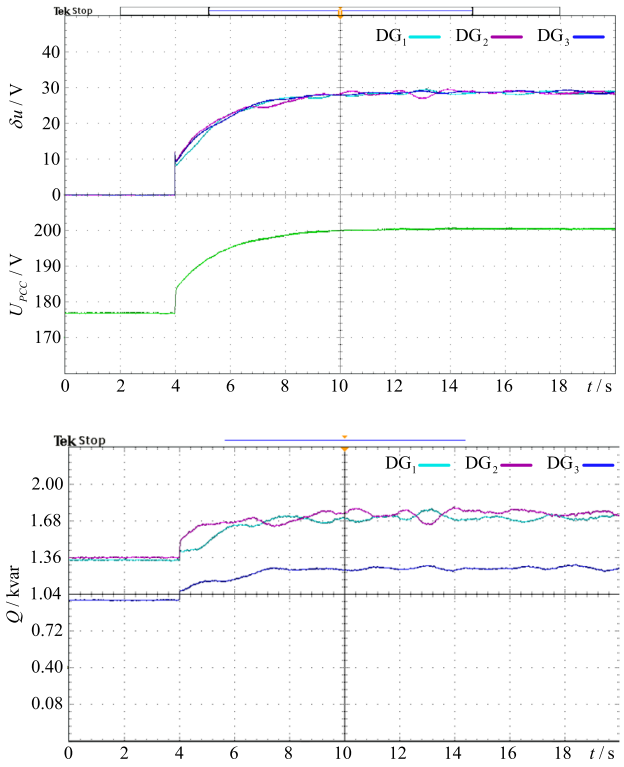

Fig. 21. Experimental waveforms of voltage compensation value δu, PCC voltage U_{PCC}, and reactive power Q of two DGs with inaccurate feeder impedance under proposed SACS-SVC.

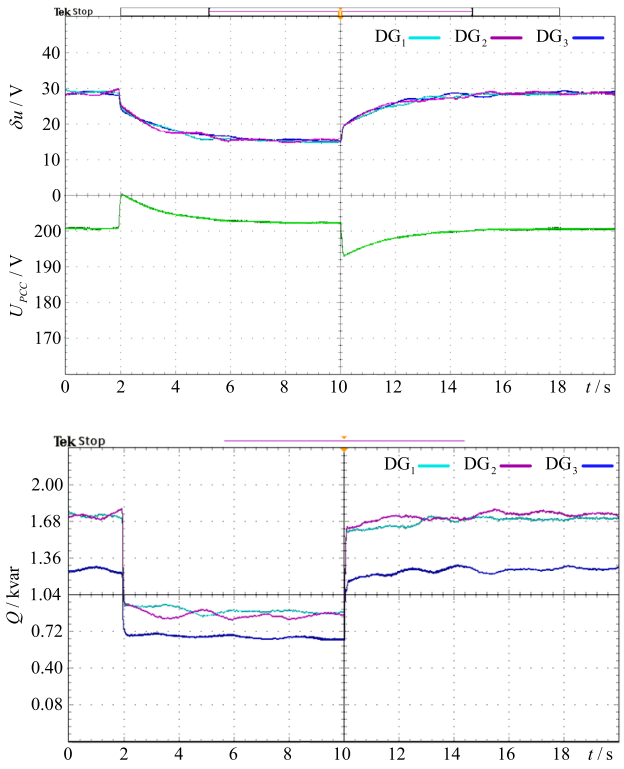

Fig. 22. Experimental waveforms of voltage compensation value δu, PCC voltage U_{PCC}, and reactive power Q of three DGs under the proposed SACS-SVC during step load changes.

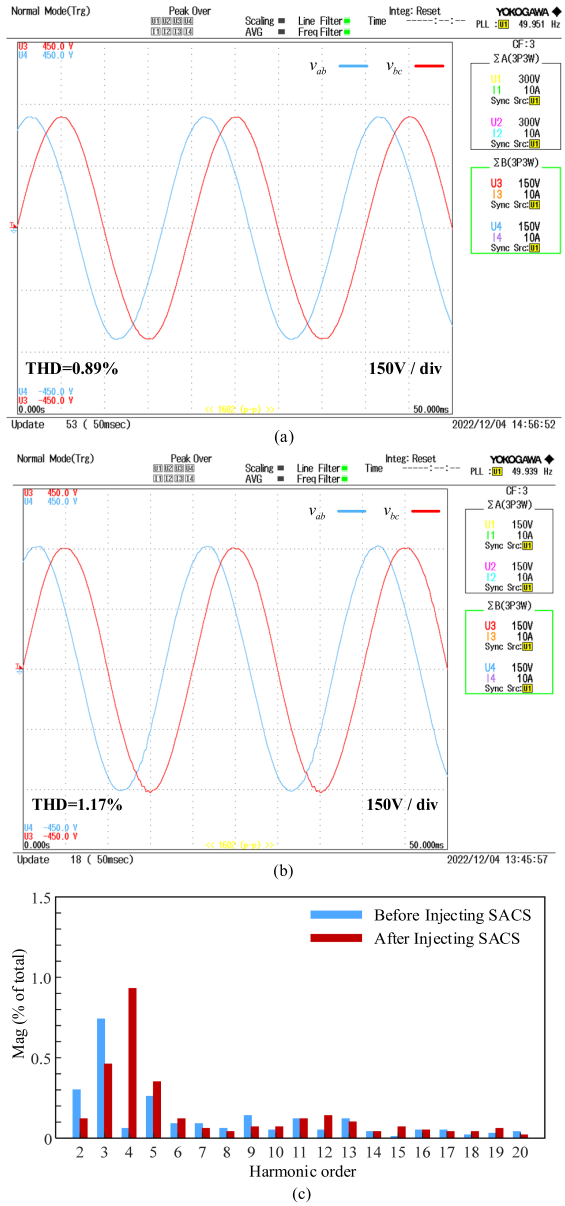

Fig. 23. Experimental waveforms of PCC voltage (a) before injecting the SACS, (b) after injecting the SACS, and (c) their THD analysis results.

VI. Conclusion

This article proposes a decentralized PCC voltage secondary voltage control method based on injection of an additional SACS for parallel inverters in islanded microgrids. In the proposed SACS-SVC method, the PCC voltage can be restored to its nominal value precisely while reactive power divergence and reactive power sharing performances deterioration in PI- SVC is avoided by building the proposed SACS droop relation between the voltage compensation value and the SACS frequency. Therefore, an appropriate voltage compensation value is guaranteed and accurately shared without any communication links. Accordingly, the proposed SACS-SVC method can endure inaccurate line impedance and different activation times for secondary

voltage control, making it a promising solution for practical microgrid applications. Additionally, a comprehensive modeling and parameter design are also presented in this article. Finally, simulation and experimental results verify the effectiveness of the proposed control method.

Note that the proposed method is just suitable for the microgrid with only one PCC. The secondary voltage control in the microgrid with more than one PCC is a higher control target, which is a multiobjective optimization problem. Therefore, it correspondingly has a greater demand of communication and computation and will be interesting to investigate in the future.

REFERENCES

[1] J. Rocabert, A. Luna, F. Blaabjerg, and P. Rodríguez, "Control of power converters in AC microgrids," *IEEE Trans. Power Electron.*, vol. 27, no. 11, pp. 4734–4749, Nov. 2012.

[2] S. Duryea, S. Islam, and W. Lawrance, "A battery management system for stand-alone photovoltaic energy systems," *IEEE Ind. Appl. Mag.*, vol. 7, no. 3, pp. 67–72, May/Jun. 2001.

[3] M. Farrokhabadi et al., "Energy storage in microgrids: Compensating for generation and demand fluctuations while providing ancillary services," *IEEE Power Energy Mag.*, vol. 15, no. 5, pp. 81–91, Sep./Oct. 2017.

[4] H. Xie, S. Zheng, and M. Ni, "Microgrid development in China: A method for renewable energy and energy storage capacity configuration in a megawatt-level isolated microgrid," *IEEE Electrific. Mag.*, vol. 5, no. 2, pp. 28–35, Jun. 2017.

[5] J. He, Y. W. Li, J. M. Guerrero, F. Blaabjerg, and J. C. Vasquez, "An islanding microgrid power sharing approach using enhanced virtual impedance control scheme," *IEEE Trans. Power Electron.*, vol. 28, no. 11, pp. 5272–5282, Nov. 2013.

[6] A. S. Vijay, N. Parth, S. Doolla, and M. C. Chandorkar, "An adaptive virtual impedance control for improving power sharing among inverters in islanded AC microgrids," *IEEE Trans. Smart Grid*, vol. 12, no. 4, pp. 2991–3003, Jul. 2021.

[7] X. Wang, Y. W. Li, F. Blaabjerg, and P. C. Loh, "Virtual-impedance-based control for voltage-source and current-source converters," *IEEE Trans. Power Electron.*, vol. 30, no. 12, pp. 7019–7037, Dec. 2015.

[8] J. M. Guerrero, J. C. Vasquez, J. Matas, L. G. de Vicuna, and M. Castilla, "Hierarchical control of droop-controlled AC and DC microgrids—A general approach toward standardization," *IEEE Trans. Ind. Electron.*, vol. 58, no. 1, pp. 158–172, Jan. 2011.

[9] Y. Khayat et al., "On the secondary control architectures of AC microgrids: An overview," *IEEE Trans. Power Electron.*, vol. 35, no. 6, pp. 6482–6500, Jun. 2020.

[10] A. Bidram and A. Davoudi, "Hierarchical structure of microgrids control system," *IEEE Trans. Smart Grid*, vol. 3, no. 4, pp. 1963–1976, Dec. 2012.

[11] W. Gu, G. Lou, W. Tan, and X. Yuan, "A nonlinear state estimator-based decentralized secondary voltage control scheme for autonomous microgrids," *IEEE Trans. Power Syst.*, vol. 32, no. 6, pp. 4794–4804, Nov. 2017.

[12] F. Guo, C. Wen, J. Mao, and Y.-D. Song, "Distributed secondary voltage and frequency restoration control of droop-controlled inverter-based microgrids," *IEEE Trans. Ind. Electron.*, vol. 62, no. 7, pp. 4355–4364, Jul. 2015.

[13] Q. Shafiee, J. M. Guerrero, and J. C. Vasquez, "Distributed secondary control for islanded microgrids—A novel approach," *IEEE Trans. Power Electron.*, vol. 29, no. 2, pp. 1018–1031, Feb. 2014.

[14] S. Asadollah, R. Zhu, and M. Liserre, "Analysis of voltage control strategies for wind farms," *IEEE Trans. Sustain. Energy*, vol. 11, no. 2, pp. 1002–1012, Apr. 2020.

[15] T.-T. Nguyen and H.-M. Kim, "Cluster-based predictive PCC voltage control of large-scale offshore wind farm," *IEEE Access*, vol. 9, pp. 4630–4641, 2021.

[16] J. He, Y. Pan, B. Liang, and C. Wang, "A simple decentralized islanding microgrid power sharing method without using droop control," *IEEE Trans. Smart Grid*, vol. 9, no. 6, pp. 6128–6139, Nov. 2018.

[17] N. Mohammed and M. Ciobotaru, "An accurate reactive power sharing strategy for an islanded microgrid based on online feeder impedance estimation," in *Proc. 46th Annu. Conf. IEEE Ind. Electron. Soc.*, 2020, pp. 2525–2530.

[18] R. Heydari, T. Dragicevic, and F. Blaabjerg, "Coordinated operation of VSCs controlled by MPC and cascaded linear controllers in power electronic based AC microgrid," in *Proc. IEEE 19th Workshop Control Model. Power Electron.*, 2018, pp. 1–4.

[19] X. Wu, C. Shen, and R. Iravani, "A distributed, cooperative frequency and voltage control for microgrids," *IEEE Trans. Smart Grid*, vol. 9, no. 4, pp. 2764–2776, Jul. 2018.

[20] Y. Xu, Q. Guo, H. Sun, and Z. Fei, "Distributed discrete robust secondary cooperative control for islanded microgrids," *IEEE Trans. Smart Grid*, vol. 10, no. 4, pp. 3620–3629, Jul. 2019.

[21] M. Hua, H. Hu, Y. Xing, and J. M. Guerrero, "Multilayer control for inverters in parallel operation without intercommunications," *IEEE Trans. Power Electron.*, vol. 27, no. 8, pp. 3651–3663, Aug. 2012.

[22] X. Huang, K. Wang, J. Qiu, L. Hang, G. Li, and X. Wang, "Decentralized control of multi-parallel grid-forming DGs in islanded microgrids for enhanced transient performance," *IEEE Access*, vol. 7, pp. 17958–17968, 2019.

[23] C. N. Rowe, T. J. Summers, R. E. Betz, and T. G. Moore, "A virtual point of common coupling voltage for improved droop control in microgrids," in *Proc. 15th Int. Power Electron. Motion Control Conf.*, Novi Sad, Serbia, 2012, pp. LS4b-2.1-1–LS4b-2.1-8.

[24] H. Moussa, J.-P. Martin, S. Pierfederici, and N. Moubayed, "Power sharing enhancement for islanded microgrid based on state estimation of PCC rms-voltage," in *Proc. 42nd Annu. Conf. IEEE Ind. Electron. Soc.*, 2016, pp. 3878–3883.

[25] M. Ciobotaru, R. Teodorescu, P. Rodriguez, A. Timbus, and F. Blaabjerg, "Online grid impedance estimation for single-phase grid-connected systems using PQ variations," in *Proc. IEEE Power Electron. Specialists Conf.*, 2007, pp. 2306–2312.

[26] M. Kosmecki and R. Rink, "Hybrid method for grid impedance estimation based on local measurements," in *Proc. IEEE 59th Int. Sci. Conf. Power Elect. Eng. Riga Tech. Univ.*, 2018, pp. 1–4.

[27] Y. Shi, Z. Liu, J. Wang, and J. Liu, "A decentralized PCC voltage secondary control method based on small-AC-signal injection for parallel inverters in islanded microgrids," in *Proc. 6th IEEE Workshop Electron. Grid*, 2021, pp. 1–7.

[28] P. L. Minh, H. P. T. Xuan, D. H. V. Duc, and H. N. Minh, "Control of power inverter in islanded microgrids based on online line impedance estimation," in *Proc. Int. Conf. Syst. Sci. Eng.*, 2017, pp. 180–185.

[29] N. Hoffmann and F. W. Fuchs, "Minimal invasive equivalent grid impedance estimation in inductive–resistive power networks using extended Kalman filter," *IEEE Trans. Power Electron.*, vol. 29, no. 2, pp. 631–641, Feb. 2014.

[30] P. Rodriguez, A. Luna, I. Candela, R. Mujal, R. Teodorescu, and F. Blaabjerg, "Multiresonant frequency-locked loop for grid synchronization of power converters under distorted grid conditions," *IEEE Trans. Ind. Electron.*, vol. 58, no. 1, pp. 127–138, Jan. 2011.

[31] J. He and Y. W. Li, "Analysis, design, and implementation of virtual impedance for power electronics interfaced distributed generation," *IEEE Trans. Ind. Appl.*, vol. 47, no. 6, pp. 2525–2538, Nov./Dec. 2011.

[32] J. C. Vasquez, R. A. Mastromauro, J. M. Guerrero, and M. Liserre, "Voltage support provided by a droop-controlled multifunctional inverter," *IEEE Trans. Ind. Electron.*, vol. 56, no. 11, pp. 4510–4519, Nov. 2009.

[33] E. A. A. Coelho, P. C. Cortizo, and P. F. D. Garcia, "Small-signal stability for parallel-connected inverters in stand-alone AC supply systems," *IEEE Trans. Ind. Appl.*, vol. 38, no. 2, pp. 533–542, Mar./Apr. 2002.

[34] N. Pogaku, M. Prodanovic, and T. C. Green, "Modeling, analysis and testing of autonomous operation of an inverter-based microgrid," *IEEE Trans. Power Electron.*, vol. 22, no. 2, pp. 613–625, Mar. 2007.

[35] *IEEE Recommended Practice and Requirements for Harmonic Control in Electric Power Systems*, IEEE Standard 519-2014 (Revision of IEEE Std 519-1992), Jun. 11, 2014. [Online]. Available: https://ieeexplore.ieee.org/document/6826459

[36] *Code on Security and Stability for Power Systems*, National Standard of the People's Republic of China GB/T 37340-2019, 2019. [Online]. Available: https://openstd.samr.gov.cn/bzgk/gb/newGbInfo?hcno=1D988D54A435E864E67CAA13217E8A99

[37] *IEEE Application Guide for IEEE Std 1547,IEEE Standardfor Interconnecting Distributed Resources with Electric Power Systems*, IEEE Std 1547-2003, pp. 1–28, Jul. 28, 2008. [Online]. Available: https://ieeexplore.ieee.org/document/1225051